

Out-of-Distribution Detection in Molecular Complexes via Diffusion Models for Irregular Graphs

David Graber^{1,2*}, Victor Armegioiu^{1*}, Rebecca Buller³, Siddhartha Mishra¹

* These authors contributed equally to this work and share first authorship. Author order was determined by coin toss.

¹ Seminar for Applied Mathematics, Department of Mathematics and ETH AI Center, ETH Zurich, 8092 Zurich, Switzerland

² Institute for Computational Life Sciences, Zurich University of Applied Sciences, 8820 Waedenswil, Switzerland

³ Department of Chemistry, Biochemistry and Pharmaceutical Sciences, University of Bern, 3012 Bern, Switzerland

Correspondence to:

David Graber (david.graber@sam.math.ethz.ch)

Victor Armegioiu (victor.armegioiu@sam.math.ethz.ch)

Prof. Dr. Rebecca Buller (rebecca.buller@unibe.ch)

Prof. Dr. Siddhartha Mishra (siddhartha.mishra@ethz.ch)

Abstract

Predictive machine learning models generally excel on in-distribution data, but their performance degrades on out-of-distribution (OOD) inputs. Reliable deployment therefore requires robust OOD detection, yet this is particularly challenging for irregular 3D graphs that combine continuous geometry with categorical identities and are unordered by construction. Here, we present a probabilistic OOD detection framework for complex 3D graph data built on a diffusion model that learns a density of the training distribution in a fully unsupervised manner. A key ingredient we introduce is a *unified continuous diffusion* over both 3D coordinates and discrete features: categorical identities are embedded in a continuous space and trained with cross-entropy, while the corresponding diffusion score is obtained analytically via posterior-mean interpolation from predicted class probabilities. This yields a single self-consistent probability-flow ODE (PF-ODE) that produces per-sample log-likelihoods, providing a principled typicality score for distribution shift. We validate the approach on protein-ligand complexes and construct strict OOD datasets by withholding entire protein families from training. PF-ODE likelihoods identify held-out families as OOD and correlate strongly with prediction errors of an independent binding-affinity model (GEMS), enabling a priori reliability estimates on new complexes. Beyond scalar likelihoods, we show that multi-scale PF-ODE trajectory statistics—including path tortuosity, flow stiffness, and vector-field instability—provide complementary OOD information. Modeling the joint distribution of these trajectory features yields a practical, high-sensitivity detector that improves separation over likelihood-only baselines, offering a label-free OOD quantification workflow for geometric deep learning.

Contents

1	Introduction	3
2	Results	5
2.1	Dataset Log-Likelihood Distributions	5
2.2	Bioinformatic Validation of OOD Log-Likelihoods	6
2.3	OOD Classification Using Trajectory Features	9
2.4	Correlation with GEMS errors	11
2.5	GEMS-based OOD Detection Baselines	13
3	Conclusions	15
4	Discussion	16
5	Method	17
5.1	Datasets	17
5.2	Diffusion Model	17
5.2.1	Background and Motivation	18
5.2.2	Unified continuous diffusion for molecular coordinates and identities	18
5.2.3	Diffusion Model Setup	20
5.2.4	Diffusion Model Training and Evaluation	21
5.3	GEMS Training and Evaluation	22
5.4	Protein-Ligand Complex Similarity Computation	23
5.5	Trajectory-aware out-of-distribution detection	24
5.6	Embedding-space baseline on GEMS	26
5.7	Rate-In baseline on GEMS	28
5.8	Author Contributions	30
5.9	Acknowledgments	30
S1	Supplementary Information	31
S1.1	Trajectory-aware OOD detection successful for 3dd0 dataset	31
S1.2	Error-log-likelihood relation	31
S1.3	Trajectory feature importance	32
S1.4	Evaluation of sensitivity to ligand size and chemical features	33
S1.5	Intra-Cluster Ligand Diversity	34
S1.6	Sampling Evaluation	35
S1.7	PF-ODE likelihoods as predictors of predictive error	35
S1.7.1	Relative entropy along the PF-ODE	36
S1.7.2	PF-ODE negative log-likelihood as a random variable	39
S1.7.3	Coupling PF-ODE likelihoods to GEMS errors	40
S1.8	Comprehensive Error Tables	41

1 Introduction

Out-of-distribution (OOD) detection is essential in machine learning, because real-world data often does not match the data distribution used for model training. In these cases, models often make overly confident predictions on the unfamiliar or shifted inputs, which can lead to serious errors, especially in high-stakes domains like diagnostics or drug discovery. Effective OOD detection provides a safeguard by identifying when a model is operating outside its reliable domain, allowing users to reject predictions or handle uncertain cases more appropriately. This not only improves safety but also builds trust in machine learning models deployed in dynamic environments.

Here we demonstrate that denoising diffusion probabilistic models (DDPMs) can serve as practical OOD detectors that can be integrated with deployed predictive machine learning models to provide a supporting confidence score and flag predictions made on input data that falls outside the model’s reliable domain. These models can be trained on any data amenable to continuous diffusion and require no labels. When trained on the same training set as a predictive machine learning model, the DDPM learns a probability density function of the training distribution. For new graphs, it can output a scalar likelihood score that indicates the degree to which new data samples match the training distribution. If presented with an OOD data point, the DDPM produces a low likelihood value, signaling that the input data point is atypical under the training distribution and that the predictive machine learning model’s output may be unreliable.

To estimate this OOD likelihood, we make use of the specific properties of DDPMs: These generative models define a continuous forward process that gradually transforms a clean input structure into pure Gaussian noise using a stochastic differential equation (SDE). Then, they learn a corresponding reverse process to travel back from noise to the original clean structure by solving the backward SDE. Importantly, the SDE that governs the noising process has a corresponding, mathematically equivalent probability-flow ordinary differential equation (PF-ODE). This deterministic ODE transports samples from the noisy state back to the clean data state while matching the probability distribution of the SDE at every intermediate time point. In other words, the ODE transforms the simple Gaussian distribution of the noise into the complex distribution of the real data. In this setting, we can estimate for any new data point how well it matches the training distribution of the diffusion model by integrating the divergence of the probability flow ODE’s drift term along the trajectory from the clean state to the terminal noisy state. The resulting log-likelihood value provides a mathematically rigorous estimator of how out-of-distribution the new data is.

We showcase the OOD detection ability of DDPMs using a database of 3D protein-ligand interaction complexes called PDBbind [1, 2]. This data combines discrete attributes (atom and residue types) with continuous spatial geometry (atom and residue positions). Therefore, these interactions are typically modeled as complex unordered graphs, making OOD detection with simple statistical checks or similarity computations impractical. Instead, we need methods that produce OOD scores based on a joint assessment of discrete and geometric graph features. DDPMs can accomplish this task, because they explicitly model the probability density of this joint distribution and are amenable to log-likelihood-based evaluation.

To train a diffusion model on this complex data and obtain a probability flow ODE for log-likelihood computation, we introduce a unified continuous diffusion framework that treats both 3D geometry and discrete chemical identities in a single Euclidean state. By mapping the categorical data onto a continuous, spherical embedding space and concatenating these chemical embeddings with the 3D spatial coordinates, we can subject the entire molecular state to a single diffusion process. A single SE(3)-equivariant graph neural network (EGNN) consumes this joint state of coordinates and noisy categorical embeddings and outputs per-node clean coordinates and probability (logits) of each chemical type. We then calculate a posterior mean (essentially a weighted average of the learned chemical prototypes based on the predicted probabilities) and compute the score analytically from this "clean" signal. This method of posterior-mean interpolation allows us to train the model using standard cross-entropy loss while maintaining the smooth, continuous dynamics required for the diffusion process. After training, the model defines a single, self-consistent probability flow ODE

whose pathwise divergence integrated in time, together with a terminal Gaussian evaluation, yields per-complex log-likelihoods.

Trained on a distribution of known protein-ligand interactions, our diffusion model allows to sample new interactions with realistic molecular structure, demonstrating successful distribution learning (Section S1.6). Crucially, it allows to estimate the in-distribution (ID) and out-of-distribution (OOD) likelihood for new interactions using its probability flow ODE. To demonstrate this ability, we constructed a custom train-test split of the PDBbind database by isolating seven protein families from the training data, thereby forming seven strict OOD test sets. We combined these test sets with two datasets exhibiting intermediate degrees of distribution shift and validated the OOD degrees of these datasets in an extensive bioinformatic analysis. For eight out of the nine datasets, the diffusion log-likelihood distributions correctly identified the dataset’s OOD level relative to the training data.

Furthermore, we hypothesized that OOD complexes induce atypical diffusion trajectories, capturing the model’s struggle to process OOD structures. Therefore, we enriched the log-likelihood signal with 18 additional descriptors extracted along the diffusion trajectory, including path tortuosity, flow stiffness, vector-field instability and energetic cost. These quantities act as trajectory-level fingerprints of how “hard” the model has to work to explain a given complex. When modeled jointly with log-likelihoods, this augmented feature space yields a substantially stronger OOD detector, which consistently distinguishes ID from OOD complexes. Notably, this augmented approach correctly classified the dataset that had previously been misidentified based on log-likelihoods alone, showing that OOD structures induce distinct dynamics in their diffusion trajectories that facilitate OOD detection.

As a prove of usability in combination with a predictive model, we train the deep-learning-based protein-ligand binding affinity prediction method GEMS [3] on the same data. GEMS showed significantly reduced accuracy on test datasets that had been flagged as OOD by our diffusion model. This demonstrates that diffusion-based OOD estimates can provide an a priori assessments of GEMS’ reliability and accuracy on given new data, based on the degree of representation of the new data in the training distribution of both models.

A central finding of this work is that, despite working in a completely unsupervised setting, the diffusion model still recovers chemically meaningful structure. The log-likelihoods assigned by its probability-flow ODE correctly rank held-out protein families as increasingly out-of-distribution, align with bioinformatically computed protein–ligand similarity scores, and correlate with the prediction errors of deterministic pre-existing models across datasets. This agreement is non-trivial: it shows that a model which only sees raw 3D interaction geometry and discrete types can reconstruct many of the same distinctions that emerge from strongly biased, affinity-supervised or hand-engineered scores. As a result, trajectory statistics collected along the probability-flow ODE provide an OOD signal that is both task-agnostic and chemically interpretable, and can serve as an independent check on the effective training distribution seen by downstream predictive models.

2 Results

A practical obstacle in structure-based machine learning is that labels are scarce, but structures are not. As of December 2025, the Protein Data Bank (PDB) contains more than 2.4×10^5 released, atomic-resolution structures, with on the order of 10^4 new structures added per year [4]. By contrast, widely used structure–affinity datasets are orders of magnitude smaller: PDBbind v2020 provides 19,443 protein-ligand complexes with curated binding affinities, and evaluation benchmarks such as CASF-2016 comprise only a few hundred labeled co-crystal complexes [5, 6].

This label-free regime is precisely where our OOD detection approach is designed to operate. Our diffusion model is trained *only* to model the joint distribution of 3D geometry and discrete atom/residue identities. It never uses binding affinities, protein-family annotations, hand-crafted similarity scores, or any OOD labels. Nevertheless, PF-ODE log-likelihoods and trajectory statistics provide a quantitative, per-complex notion of *typicality* with respect to the training distribution. In the next sections we show that this label-free signal identifies held-out protein families as OOD and anticipates the error profile of an *independent* affinity predictor trained with supervision.

To evaluate the diffusion model’s OOD detection capability, we used a custom data split of the PDBbind (v.2020) dataset following the procedure of [7]. We constructed seven OOD test sets by isolating entire protein families from the dataset. The remaining data was subjected to CleanSplit filtering [3] and randomly split into training and validation sets. The filtering allowed us to include CASF2016 as an additional test set without data leakage. This resulted in a total of nine non-training datasets representing a spectrum of distribution shifts relative to the training data: The validation set, drawn from the same distribution, should exhibit minimal shift. The CASF2016 dataset occupies an intermediate position. While originally sampled from the training data, CleanSplit filtering removed structural overlaps, likely inducing a moderate shift. The largest shifts are expected for the datasets of isolated protein families, denoted by their cluster centers 1nvq, 1sqa, 2p15, 2vw5, 3dd0, 3f3e, and 3o9i. Following training of the diffusion model, we computed log-likelihoods and 18 additional PF-ODE trajectory statistics across all datasets and evaluated the discriminative power of these features in detecting OOD inputs.

2.1 Dataset Log-Likelihood Distributions

The log-likelihoods assigned to the training, validation, and OOD datasets generally aligned with expectations (Figure 1). As anticipated, the training dataset received high log-likelihoods, showing that this dataset fits the distribution learned by the diffusion model. The validation dataset received log-likelihoods slightly lower than the training set, which is expected for unseen samples drawn from the training distribution. The OOD datasets composed of extracted protein family clusters mostly yielded low log-likelihoods, indicating they were correctly identified as OOD. Finally, the CASF2016 dataset produced log-likelihoods intermediate to the training and OOD datasets. This aligns with the nature of the CleanSplit filtering used to ensure the independence of CASF2016: While it removes high-similarity complexes, it does not enforce the strict independence achieved by holding out entire protein families. Among the OOD datasets, the HIV protease family showed the most pronounced distribution shift in log-likelihoods relative to the training data. This finding aligns with biological expectations, as HIV protease complexes possess unique characteristics. These viral proteases contain an active site located between two short identical subunits, flanked by flexible molecular flaps that close upon substrate binding. Inhibitors targeting these enzymes are typically large molecules designed to mimic the proteolytic transition state without being cleaved, effectively blocking the active site. A significant deviation from biological expectation occurred in one of the nine datasets. The carbonic anhydrases in the 3dd0 cluster yielded high log-likelihoods, suggesting that this dataset is in-distribution relative to the training data. We focus our evaluation of the PF-ODE log-likelihoods on the remaining eight datasets and discuss the 3dd0 results separately in Sections 2.3, S1.1 and S1.4.

Log-Likelihood Variance The distributions of log-likelihoods (Figure 1) were broad across all datasets. This variance is expected for the inherently diverse training and validation datasets, but also for CASF2016 dataset, which is diverse by design. OOD datasets generally showed lower variance in

log-likelihoods. Nevertheless, a considerable spread remained also in the OOD datasets, suggesting that these datasets still contain typical as well as atypical complexes. This is likely attributable to our splitting strategy: While we sequestered specific protein families, the ligand space remained uncontrolled. Consequently, OOD pockets may bind a diverse mix of ligands, ranging from familiar to exotic structures, which naturally drives variation in the likelihood scores. The impact of ligand diversity on log-likelihood spread becomes evident by analyzing the ligand size distribution and chemical diversity within the datasets (Figures S3 and S6). For every dataset, we identified a medoid ligand, defined as the molecule with the smallest sum of distances ($1 - \text{Tanimoto similarity}$) to all other ligands, and computed the distance of all other ligands to this central reference. We found a strong correlation between cluster tightness (median distance to the medoid) and the standard deviation of the log-likelihood distributions (Pearson’s $r = 0.832$). This shows that datasets with diverse sets of ligands exhibited the broadest log-likelihood distributions. The most extreme case is the cluster of transporter protein binding pockets 3f3e, which exhibits a ligand size distribution much broader than all other datasets (Figure S3).

2.2 Bioinformatic Validation of OOD Log-Likelihoods

To validate the OOD log-likelihoods obtained from the diffusion model, we performed an extensive bioinformatic analysis, evaluating the degree of representation of the validation, CASF2016 and OOD datasets in the training distribution. First, we computed pairwise similarities across all 19’443 complexes in PDBbind using a combined assessment of protein similarity (TM-align [8]), ligand similarity (Tanimoto scores [9]) and binding conformation similarity (pocket-aligned ligand RMSD). Tanimoto similarity is commonly used to measure the similarity between small molecules. Based on comparing chemical fingerprints, this score ranges between 0 (no similarity) and 1 (identical) and identifies compounds with similar structural and chemical properties. TM-align compares protein structures by finding the optimal alignment of their three-dimensional shapes, producing a TM-score ranging from 0 (very dissimilar fold) to 1 (identical fold). The pocket-aligned ligand RMSD calculation completes the similarity assessment by comparing ligand positioning within aligned protein pockets (based on TM-align). For each metric, we computed all $189 * 10^6$ pairwise similarities across PDBbind and generated individual pairwise similarity matrices. Combining these three metrics allows for a robust structure-based similarity quantification between protein-ligand complexes.

We approximated the degree of representation of the non-training datasets within the training data by quantifying the number and the magnitude of similarities shared between the training complexes and the respective non-training datasets. We then aligned these similarity results with the log-likelihood distributions obtained from the diffusion model (Figure 2).

- **TM scores** aligned closely with the log-likelihood distributions (Figure 2a, c). Datasets sharing fewer and weaker similarities in protein folds with the training data exhibit lower log-likelihoods (suggesting more OOD). While validation set proteins were well-represented within the training data, the CASF2016 proteins shared only moderate structural similarity. The proteins of the OOD datasets were highly underrepresented in the training data, confirming that the pocket-level splitting mechanism effectively isolates proteins with distinct folds (Figure 2c).
- **Tanimoto scores** showed a slightly weaker correlation with the log-likelihood distributions (Figure 2a, b). Nevertheless, a similar trend persisted: Datasets sharing weaker ligand similarities with the training set yield lower log-likelihoods. The OOD datasets showed significantly lower similarity to the training data than the validation set. This confirms that isolating specific protein types during OOD splitting automatically induces a moderate shift in the ligand distribution.
- **Aggregated similarity scores** were derived by computing the sum of Tanimoto, TM-align, and inverted RMSD scores for each pair of complexes. The aggregated similarity scores between two datasets offer a more complete measure of independence, as it accounts for protein, ligand and binding pose similarity simultaneously. The number and magnitude of shared similarities aligned well with the log-likelihood distributions (Figure 2a, d). Datasets with complexes sharing fewer and weaker similarities with the training data obtained lower log-likelihoods.

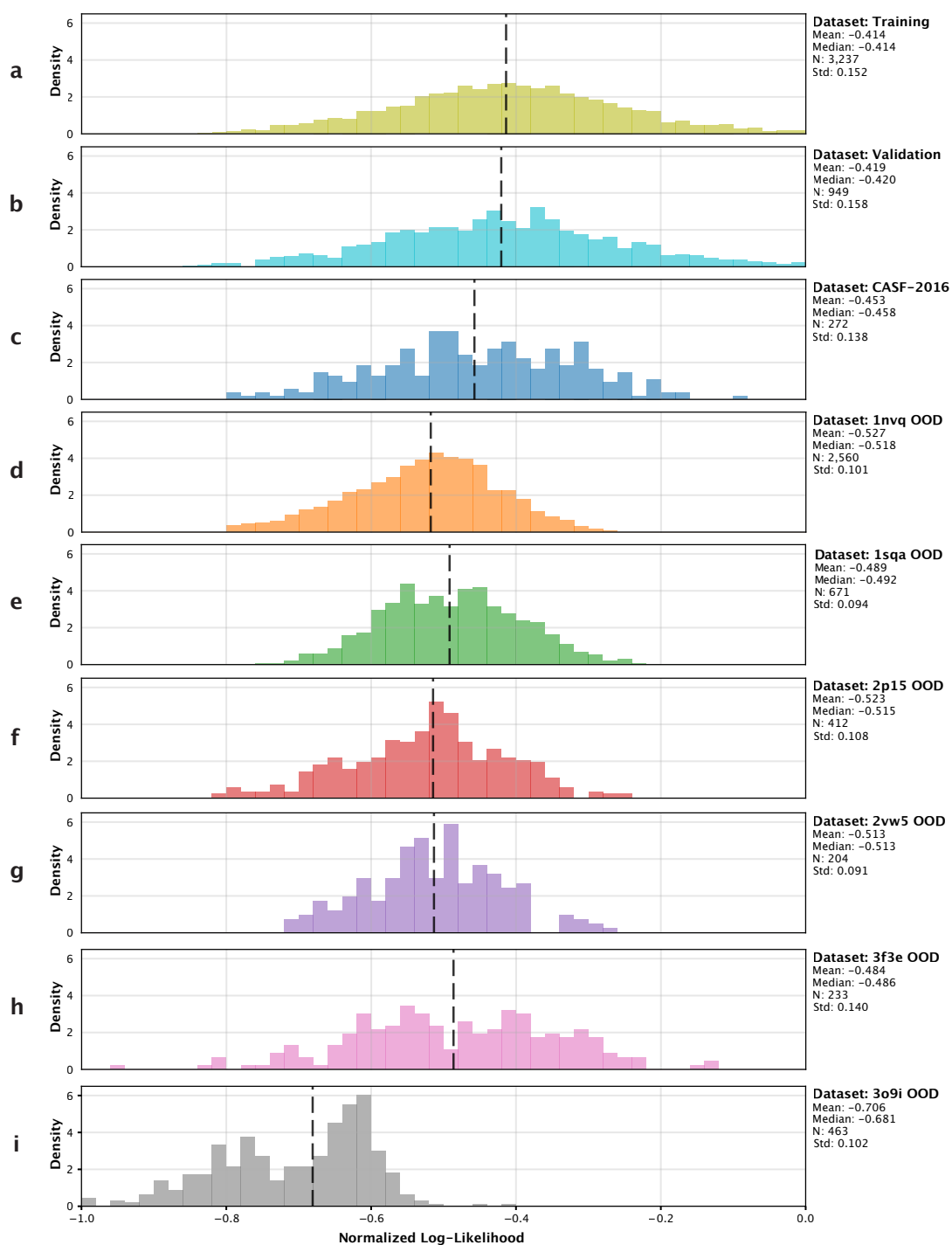


Figure 1: Out-of-distribution datasets yield lower log-likelihoods: Distributions of log-likelihoods assigned to protein-ligand complexes belonging to the a) training, b) validation, c) CASF2016 and the out-of-distribution (OOD) datasets d) 1nvq, e) 1sqa, f) 2p15, g) 2vw5, h) 3f3e and i) 3o9i. Lower values signify increased deviation from the learned distribution (OOD) and higher values indicate high in-distribution (ID) probability. Means, medians, standard deviations (Std) and number of samples (N) are depicted on the right side of the histograms. Vertical dashed lines indicate the median of the respective log-likelihood distributions. Distributions were subjected to individual outlier removal using the IQR method ($1.5 \times \text{IQR}$ rule) followed by min-max normalization to a $[-1, 0]$ range using global minimum and maximum values across all distributions. The training distribution was randomly subsampled, showing only a fraction of all 10^5 complexes.

While the magnitude of Tanimoto and TM scores shared between training and non-training datasets certainly influences the log-likelihood distributions, these metrics should not be taken as a direct proxy for the number of similar complexes shared between them. This is because similar protein folds may be associated with entirely different ligands, and structurally similar ligands might bind to completely disparate proteins, thereby resulting in the absence of similarity at the protein–ligand interaction level. Only the combination of these metrics at the complex level, combined with a supplementary assessment of binding conformation similarity, can accurately quantify the structural overlap between two datasets. This combined assessment demonstrates that all designed OOD datasets share fewer and weaker complex-level similarities with the training data: For many training complexes, no representation of the same binding pattern is found in these datasets whatsoever (aggregated similarity scores at zero). The similarity scores of the CASF2016 dataset confirm that the CleanSplit filtering applied to the training data renders the CASF2016 dataset more independent, without reaching the same strict level of independence achieved by the OOD benchmarks.

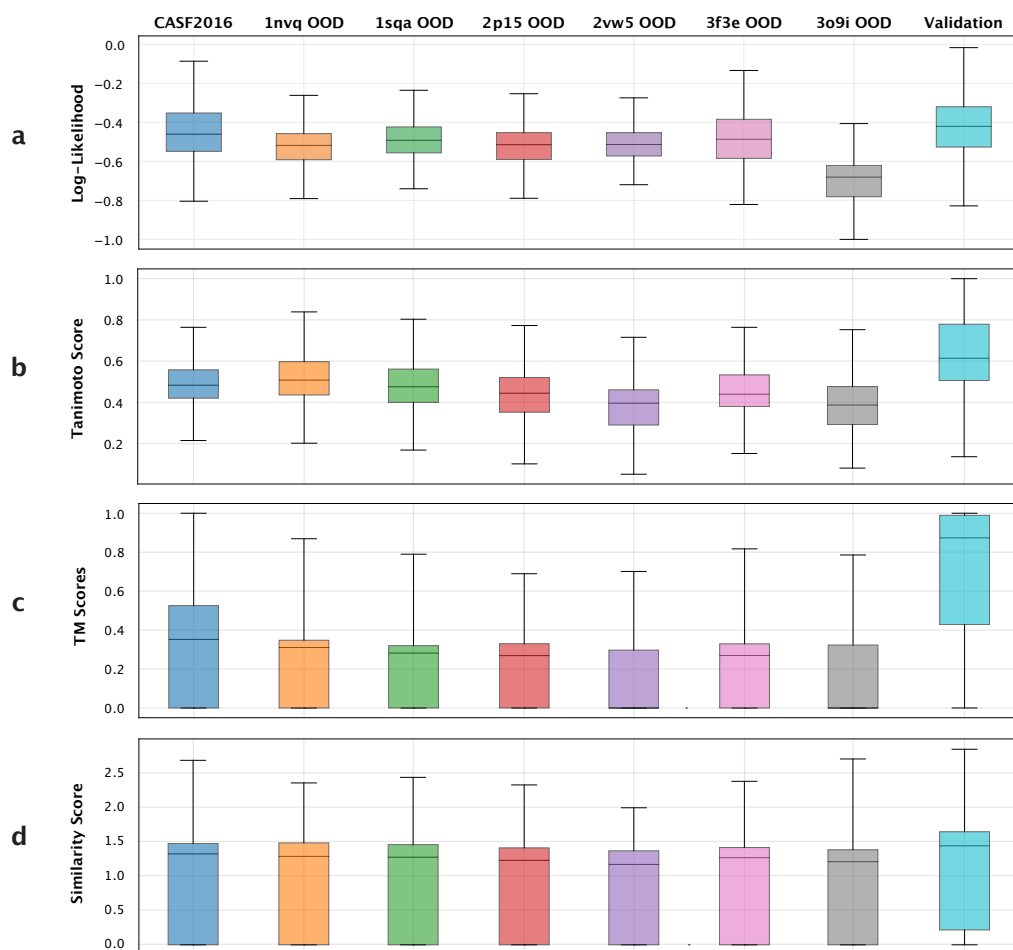


Figure 2: Log-likelihood distributions align with protein and ligand similarity metrics: Comparison of the distributions of **a)** log-likelihoods assigned by the diffusion model with the distributions of train-test similarity scores (**b**, **c** and **d**). **b)** Ligand Similarity: Calculated using Tanimoto scores between count-based molecular fingerprints. High scores indicate high similarity (1.0 = identical). **c)** Protein Similarity: Determined by TM-align based on optimal 3D protein structure alignment. High scores indicate high structural similarity (1.0 = identical) **d)** Aggregated Similarity: A composite score $S = \max(\text{Tanimoto} + \text{TM Score} + (1 - \text{RMSD}), 0)$ was calculated as the sum of Tanimoto similarity, TM-scores, and inverted pocket-aligned ligand root mean squared deviation (RMSD). High scores signify highly similar protein-ligand complexes (3.0 = identical complexes). Each box (**b**, **c** and **d**) represents the distribution of $N = 10,510$ similarity scores. Specifically, these are the scores between each training dataset complex and its most similar counterpart in the respective test dataset, as measured by that specific metric. Boxplots show the median (centre line), 25th–75th percentiles (box), whiskers extend to data points within $1.5 \times \text{IQR}$, outliers are not shown.

Across the eight datasets evaluated, the log-likelihood values assigned by the diffusion model align closely with the bioinformatic similarity estimates. This validation suggests that the PF-ODE log-likelihood distributions have a basis in the underlying structural and chemical similarity between the training and non-training datasets and that log-likelihood values are indicative of the degree of out-of-distribution of new data. However, despite this alignment, the log-likelihood distributions retained significant overlap with the training data, making robust separation by a classifier difficult. Consequently, we concluded that log-likelihoods alone are insufficient for reliable OOD detection. To address this, we incorporated additional PF-ODE trajectory statistics designed to capture the diffusion model’s struggle to process OOD data.

2.3 OOD Classification Using Trajectory Features

We introduce a novel methodology for OOD detection that leverages the full information in a sample’s noising trajectories for accurate OOD classification. Instead of relying solely on the final scalar log-likelihood, we collect 18 additional trajectory statistics that characterize the model’s dynamical behavior when transforming an input structure into Gaussian noise.

- **Geometric Inefficiency:** Path tortuosity and its inverse, path efficiency, characterize the extent to which the trajectory wanders or deviates from a direct path. Increased tortuosity is an indicator of distribution shift and OOD, suggesting the model struggles to maintain a geometrically efficient path in high-dimensional space.
- **Local Instability and Stiffness:** The maximum Lipschitz estimate reads off flow stiffness. High values indicate that nearby states elicit disproportionately different drifts, signaling that the model is operating off-manifold.
- **Vector Field Activity and Smoothness:** The vector-field mean and a spikiness ratio quantify the magnitude and burstiness of corrective pushes required by the model. Mean acceleration records the lack of temporal smoothness, indicating abrupt changes in the flow’s velocity.
- **Energetic Cost:** Total flow energy, aggregated along the trajectory path, captures the total directed "work" expended by the model.

These additional features show coordinated variation under distribution shift caused by OOD samples: Stiff, bursty vector fields, higher acceleration and longer, less efficient paths tend to co-occur when processing OOD samples. Therefore, including quantities describing this coordinated movement facilitates robust OOD classification. We showcase this trajectory-aware OOD-detection approach using our protein-ligand datasets.

Classifier Setup For each molecular complex, we collect a scalar log-likelihood and the 18 additional trajectory statistics, forming a $d = 19$ -dimensional feature vector describing the complexity, stability, and efficiency of the flow dynamics. To obtain an OOD detector, this set of trajectory features is subsequently used to fit separate Gaussian Kernel Density Estimators (KDEs) for in-distribution (ID) and OOD samples. To obtain an OOD score for new data, we derive a negated Log-Density Ratio (LDR), where larger scores indicate higher confidence that the sample is OOD. A binary classification is achieved by thresholding, optimized on a validation set (see Methods). To obtain a robust and balanced performance estimate despite class imbalance, we employ a bootstrap evaluation strategy. For each OOD split we partition ID and OOD complexes into training, validation, and test subsets. The PCA and the two KDEs are fit on their respective training data, and the decision threshold is fixed once by maximizing the F1-score for the OOD class on the validation set. Because the number of ID decoys can be much larger than the number of OOD binders, naive evaluation on the full test pool would overweight specificity. To obtain a balanced and robust estimate, we keep the OOD test set fixed and repeatedly draw balanced ID test subsets of the same size. For each draw we evaluate the classifier, treating OOD as the positive class, and record AUROC, accuracy, precision, recall, F1 and specificity.

Dataset	AUROC	Accuracy
casf2016	0.708 \pm 0.042	0.604 \pm 0.029
1nvq	0.842 \pm 0.013	0.744 \pm 0.011
1sqa	0.888 \pm 0.013	0.787 \pm 0.014
2p15	0.754 \pm 0.034	0.693 \pm 0.027
2vw5	0.939 \pm 0.033	0.888 \pm 0.028
3dd0	0.951 \pm 0.009	0.956 \pm 0.009
3f3e	0.639 \pm 0.061	0.598 \pm 0.035
3o9i	0.963 \pm 0.006	0.949 \pm 0.011

Table 1: Trajectory-aware OOD classifier performance: Comparison of AUROC and accuracy across OOD datasets for the trajectory-aware LDR diffusion-based detector. To obtain a robust and balanced performance estimate despite class imbalance, we employ a bootstrap evaluation strategy. We keep the OOD test set fixed and repeatedly draw 100 balanced ID subsets of the same size from the training data. For each draw we evaluate the classifier, treating OOD as the positive class and report the mean \pm standard deviation over the balanced bootstrap subsets.

Performance Evaluation The classifier demonstrated robust performance on samples with strong distribution shifts relative to the training data (Table 1 and S3), achieving consistent separation on the most structurally unique OOD data such as HIV-proteases (3o9i) and heat-shock-proteins (2vw5). However, as anticipated, accuracy diminished on datasets with intermediate OOD characteristics, confirming that these datasets contain complexes that retained moderate similarity to the training data and are therefore hard to separate. A prime example is the CASF2016 benchmark: Originally sampled from the training distribution, this dataset was rendered more independent via CleanSplit filtering. Consequently, it occupies a OOD space between the training data and the OOD datasets, as confirmed by both log-likelihood profiles and bioinformatic similarity analysis (Figure 2). This moderate distribution shift resulted in the low OOD-classification accuracy. Similarly, the transporter protein dataset (3f3e) was predicted with low accuracy. This dataset equally showed intermediate OOD characteristics. Its log-likelihood distribution was very broad with significant overlap with the training log-likelihoods, a finding that was further confirmed with bioinformatic metrics showing a significant degree of retained structural similarity with the training data (Figure 2).

To assess the contribution of the trajectory features to the strong discriminative power of the OOD detector, we computed feature importance scores (Figure S2). While the PF-ODE log-likelihoods was most important for classification, we found a significant contribution of the additional trajectory descriptors to the OOD detector’s performance – the precise details are fleshed out in Section S1.3. Especially path stability, vector field burstiness and drift smoothness notably contribute to the OOD classification performance. Compared to a classifier based on PF-ODE log-likelihoods only, the classifier integrating additional trajectory descriptors achieved significantly more accurate OOD classification.

Trajectory features rescue 3dd0 classification One of the nine non-training datasets (3dd0, containing alpha-carbonic anhydrases) yielded unexpectedly high PF-ODE log-likelihoods. Relying on these scores alone would result in the erroneous classification of this dataset as in-distribution (Figure S4). However, our results demonstrate that augmenting the log-likelihoods with additional trajectory statistics sufficiently enriches the feature space to correct this prediction and flag the dataset as OOD. This ensemble of trajectory features enabled the construction of a robust decision boundary between the training data and the alpha-carbonic anhydrase structures, effectively compensating for the lack of discriminative signal in the raw likelihood scores.

These observations made on our protein-ligand data show that modeling the joint behavior of several trajectory features yields substantially stronger OOD detection accuracy compared to methods that rely solely on the trajectory log-likelihoods. This confirms that these trajectory statistics provide critical, complementary signals that are characteristic fingerprints of out-of-distribution processing. While we demonstrated the power of this approach using protein–ligand complexes, a challenging domain of unordered 3D graphs, the implications extend far beyond molecular biology. This detection framework, using a set of 19 trajectory features, is universally applicable to any data modality amenable to continuous diffusion modeling. On top, due to the purely generative training objective, no data labels are required.

2.4 Correlation with GEMS errors

To assess whether log-likelihoods can predict the performance of predictive models, the binding affinity prediction model GEMS was trained on the same data split. This Graph Neural Network (GNN) processes graph representations of protein-ligand interaction patterns within a complex and performs regression to predict a scalar binding affinity value (pK). Although the diffusion model and GEMS are independent, the log-likelihoods assigned by the diffusion model to the training, validation, and test datasets generally align with the performance metrics achieved by GEMS on the same datasets. The binding affinity prediction R^2 of GEMS showed a strong correlation with the median log-likelihoods of the same dataset (Pearson Correlation Coefficient, $PCC = 0.750$). Similar correlations were observed for the ranking performance of GEMS, with Kendall (Tau, $PCC = 0.612$) and Spearman Correlation (Rho, $PCC = 0.613$) coefficients correlating significantly with log-likelihoods (Figure 3).

Across the eight datasets evaluated, the mean binding affinity prediction errors of GEMS significantly correlated with the median log-likelihoods assigned by the diffusion model to those same datasets ($PCC = -0.880$). Datasets assigned high median log-likelihoods consequently exhibit low mean prediction errors. Conversely, lower log-likelihood distributions are associated with a very steep increase in GEMS prediction errors (Figure 4). Regarding complex-wise errors, complexes with low log-likelihoods tend to be predicted with large errors by GEMS, while those with higher likelihoods yield lower errors. To describe this relationship, we performed a hierarchical fitting of five exponential curves (main fit, above fit, above-above fit, below fit, and below-below fit) to the log-likelihood-error relationship across a fixed number of samples drawn from all non-training distributions. This fitting confirmed that the relationship follows an approximate exponential behavior (Figure S1), showing that complex-wise log-likelihoods provide a rough estimate of the expected error for GEMS binding affinity predictions.

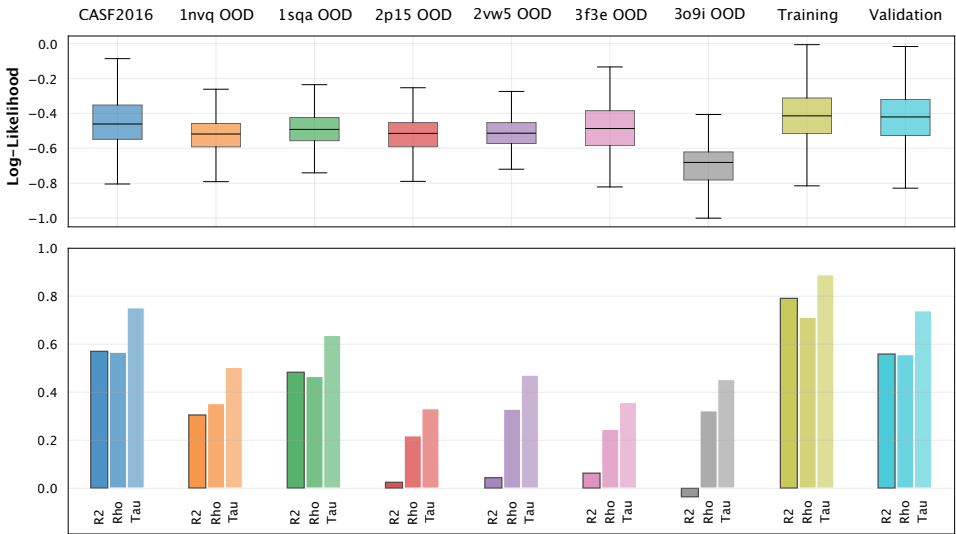


Figure 3: Correlation between log-likelihoods and GEMS performance: Comparison of log-likelihood distributions obtained for training, validation, CASF2016 and out-of-distribution (OOD) datasets with performance metrics achieved by the GEMS binding affinity prediction model trained on the same data. The box plot shows the distribution of log-likelihoods assigned to each dataset’s protein-ligand complexes by the diffusion model, where lower values signify increased deviation from the learned distribution (OOD) and higher values indicate high in-distribution probability (IID). The bar plot shows the corresponding performance metrics that GEMS achieved on the same datasets, including R-squared (R2), Kendall (Tau) and Spearman (Rho) rank correlation coefficients. Boxplots show the median (centre line), 25th–75th percentiles (box), whiskers extend to data points within $1.5 \times IQR$, outliers are not shown.

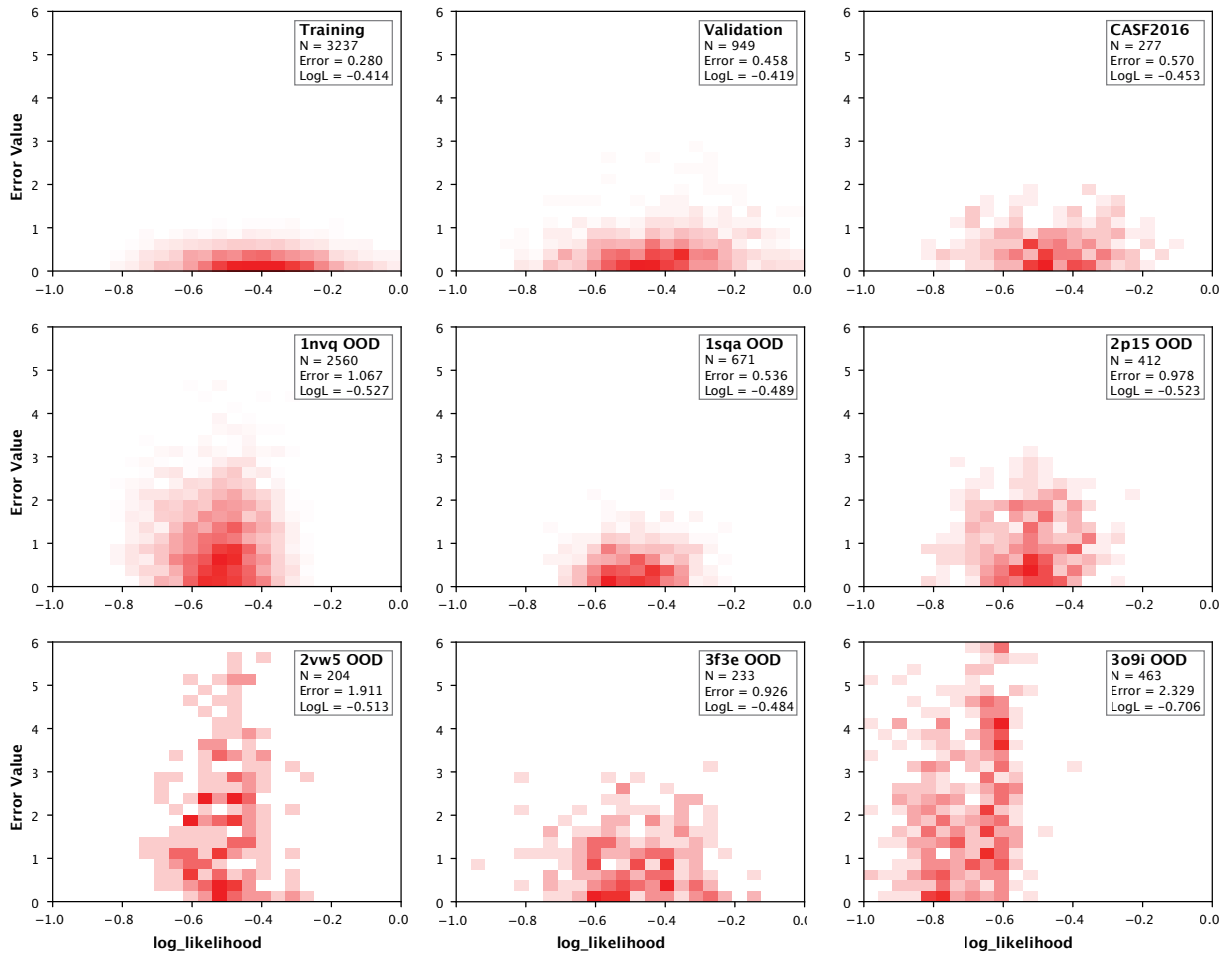


Figure 4: Out-of-distribution complexes yield higher GEMS errors: Heatmaps illustrating the relationship between the log-likelihoods assigned by the diffusion model and the corresponding GEMS binding affinity prediction errors (y-axis) across the training, validation, CASF2016 and out-of-distribution (OOD) datasets. The x-axis represents the log-likelihood for each complex, where lower values signify increased deviation from the learned distribution (OOD) and higher values indicate high in-distribution probability (ID). The y-axis represents the variance-normalized errors of the GEMS binding affinity prediction. Color intensity represents density, with white areas containing no data. To allow fair comparison across datasets with different label spreads, absolute errors are normalized by the label variance, preventing artificially low error values on narrowly distributed datasets. The heatmaps visually confirm that low log-likelihoods are associated with higher GEMS prediction errors.

PF-ODE likelihood as a typicality and risk signal To strengthen our observation that PF-ODE log-likelihoods are predictive of the performance of other predictive models that have been trained on the same data, we established a formal link between the PF-ODE log-likelihood and the reliability of predictions made by GEMS and show that the log-likelihoods control the error of the downstream model with high probability.

We interpret the PF-ODE negative log-likelihood $L(x)$ as a task-agnostic typicality score under the diffusion density q_ϕ learned from in-distribution (ID) complexes.

$$L(x) := -\log q_\phi(x),$$

Empirically, this typicality is also predictive of downstream reliability: complexes with unusually large $L(x)$ (low likelihood under q_ϕ) tend to incur larger binding-affinity errors under GEMS (Figs. 4–S1). The key intuition is that if prediction error grows (roughly) monotonically as inputs become less typical, then concentration of $L(x)$ under the ID law immediately yields a high-probability error guarantee. This is the content of the following informal proposition:

Proposition 2.1 (Likelihood controls error with high probability). *Let $x \sim p_{\text{ID}}$ and define $L(x) = -\log q_\phi(x)$ with typical value $L_{\text{typ}} = \mathbb{E}_{\text{ID}}[L(x)]$. Assume $L(x)$ has finite ID variance $\text{Var}_{\text{ID}}(L(x)) \leq \sigma^2$,*

and that there exists a non-decreasing calibration curve ϕ such that $e_\theta(x) \leq \phi(L(x))$ for (almost) all x . Then, for any margin $\alpha > 0$,

$$\mathbb{P}_{\text{ID}}(e_\theta(x) > \phi(L_{\text{typ}} + \alpha)) \leq \frac{\sigma^2}{\alpha^2}, \quad (2.1)$$

equivalently $\mathbb{P}_{\text{ID}}(e_\theta(x) \leq \phi(L_{\text{typ}} + \alpha)) \geq 1 - \sigma^2/\alpha^2$.

In practice, ϕ is obtained by fitting a monotone upper envelope to the empirical $(L(x), e_\theta(x))$ scatter on a held-out calibration set (Fig. S1), turning PF-ODE likelihoods into a quantitative, label-free risk stratifier for supervised affinity prediction. The Supplementary Material (Section S1.7) gives the formal statement (Theorem S1.9) and the broader PF-ODE context underlying this bound.

2.5 GEMS-based OOD Detection Baselines

Embedding Space Baseline To rigorously benchmark our trajectory-aware OOD detection method, we compared it against a family of classical anomaly detectors operating on the fixed latent representations of the pretrained GEMS encoder. We treated the GEMS encoder as a static feature extractor and assumed that ID complexes occupy a relatively compact region of the GEMS representation space, and that OOD complexes are either geometrically distant from this region or sparsely supported. For every molecular complex, we computed a summary embedding by averaging the output vectors from multiple stochastic forward passes of GEMS. We then trained five unsupervised anomaly detectors on these standardized ID embeddings, covering distance-based, density-ratio, isolation-based and margin-based approaches:

- Mahalanobis Distance: Measures the distance of a sample from the ID class mean, accounting for covariance.
- k-Nearest Neighbors (k-NN): Scores anomaly based on the average distance to the nearest ID training examples.
- Local Outlier Factor (LOF): Detects samples with lower local density compared to their neighbors.
- Isolation Forest: Assigns higher anomaly scores to points that are easily isolated (few splits) in random decision trees.
- One-Class SVM: Learns a decision boundary (margin) that encloses the ID data.

All classifiers were trained on the same fixed GEMS latent representations. Performance was estimated following the same rigorous evaluation protocol as with our trajectory-aware OOD detection classifier, using balanced bootstrap test subsets to ensure robustness against class imbalance (Section 2.3). As a main performance readout and robust indicator of detector quality, we compute the threshold-free AUROC (Table 2). Additionally, we calibrate decision thresholds for each OOD dataset on held-out validation sets (maximizing F1-score). We then report the performance of the detector with the highest AUROC for each dataset (Table S2).

Adaptive Uncertainty Baseline (Rate-In) To benchmark our method against state-of-the-art uncertainty estimation techniques, we implemented Rate-In [10], a dynamic baseline that is built on the concept of Monte Carlo dropout. Instead of a fixed global dropout rate, Rate-In applies adaptive, per-sample, per-layer dropout rates chosen to preserve information flow through the network. It works under the assumption that ID samples allow for relatively high dropout rates without disrupting the computation, whereas OOD inputs are more fragile and lose information under dropout perturbations. We integrated this adaptive scheme directly into the GEMS binding affinity predictor. For each molecular complex, the method iteratively optimizes the dropout intensity at every network layer, seeking the maximum dropout level that still preserves stable information flow. This process generates a sample-specific robustness profile. The final anomaly score is constructed by aggregating three distinct signals: The standard predictive variance (epistemic uncertainty), the heterogeneity of the optimized dropout rates across layers, and the computational effort (convergence difficulty) required to find these stable rates. High instability in these metrics indicates that the predictive model struggles to process the input structure, suggesting the input is OOD.

Dataset	Traj-LDR (diffusion)	GEMS (embedding)	Rate-In
casf2016	0.708 ± 0.042	0.554 ± 0.019	0.444 ± 0.041
1nvq	0.842 ± 0.013	0.804 ± 0.007	0.581 ± 0.013
1sqa	0.888 ± 0.013	0.928 ± 0.008	0.664 ± 0.024
2p15	0.754 ± 0.034	0.721 ± 0.017	0.541 ± 0.039
2vw5	0.939 ± 0.033	0.659 ± 0.033	0.439 ± 0.047
3f3e	0.639 ± 0.061	0.919 ± 0.009	0.741 ± 0.032
3o9i	0.963 ± 0.006	0.922 ± 0.010	0.859 ± 0.024

Table 2: Comparison of AUROC (mean \pm standard deviation) across OOD datasets for the trajectory-aware LDR diffusion-based detector (Traj-LDR), the embedding-space GEMS baseline, and the Rate-In baseline. All values are taken from Tables S3, S2, and S4. The `validation` split used only for Rate-In is omitted here.

Performance Evaluation These baselines establish a rigorous reference for evaluating our trajectory-aware method. While Rate-In provides a sophisticated measure of predictive uncertainty, our empirical analysis showed that it offered lower discrimination accuracy compared to the trajectory-aware OOD classifier approach (Table S4). This demonstrates that probing the stability of a discriminative model is inferior to the sensitivity of the diffusion-based approach using multiple PF-ODE trajectory features. Similarly, the embedding space baseline showed lower OOD detection accuracy across most datasets, showing that the latent space features from the GEMS encoder possess less OOD separability than the descriptors extracted from the PF-ODE trajectory.

Key distinctions from baselines The bioinformatic similarity analysis (Sections 2.2) and the GEMS-based OOD detection baselines (Section 5.6) provide a strong reference for our trajectory-aware OOD detection. However, our diffusion-based OOD detector occupies a fundamentally different region in the design space than the deterministic baselines. The diffusion model is trained in a purely generative fashion. It only observes bare three-dimensional coordinates and discrete atom/residue identities, and its objective is to approximate the joint data distribution. It never sees binding affinity labels, similarity scores, or any task-specific supervision. By contrast, our baselines are heavily endowed with biochemical priors: The bioinformatic OOD approximations are hand-crafted around well-established notions of structural and chemical similarity like TM-scores, Tanimoto scores and ligand RMSD values. In the Embedding Space baseline, OOD decisions are based on a static snapshot of the GEMS representation geometry. Similarly, the Rate-In baseline makes use of the pretrained weights of the GEMS model and derives OOD scores by probing prediction stability under dropout perturbation.

In this sense, the diffusion model is substantially more structure-agnostic than the baselines, yet it is asked to solve a more demanding problem (full generative modelling) from strictly weaker supervision. Nevertheless, the OOD detection with diffusion trajectory features outperforms all baselines in our task of recognizing OOD datasets of isolated protein families (Table 2).

Moreover, the scope of the baseline methods employed here is inherently limited. The bioinformatic approximation of OOD scores requires exhaustive pairwise comparisons to construct similarity matrices. Both the Rate-In and the Embedding Space baseline rely on a high-quality GEMS encoder trained directly on the binding affinity task. Consequently, their applicability is restricted to supervised settings where such pretrained models exist. In contrast, our OOD detector based on diffusion PF-ODE trajectory is trained in a generative fashion and requires no labels. It only exploits the diffusion model’s own internal dynamics and thus provides a versatile, label-free mechanism for OOD detection that is applicable to diverse data types and training regimes.

3 Conclusions

We introduced a diffusion-based framework for quantifying out-of-distribution (OOD) structure in irregular 3D graph data, instantiated on protein–ligand complexes. Reliable deployment of predictive models in structural biology and drug discovery requires knowing when a new complex lies outside the effective support of the training data. Our central finding is that a generative model trained only on raw 3D geometry and discrete biochemical types can provide a principled, task-agnostic OOD signal in its dynamic noising trajectories, and that this signal is strongly informative about the reliability of an independent binding-affinity predictor.

Methodologically, we use a unified continuous diffusion process that treats 3D coordinates and discrete atom/residue identities in a single Euclidean state, with categorical types embedded on an L2-normalised sphere. Posterior–mean interpolation turns logits into continuous scores, yielding a stable SE(3)-equivariant denoiser whose probability–flow ODE (PF-ODE) defines per-complex log-likelihoods. These PF-ODE likelihoods align well with bioinformatic similarity measures. Moreover, they correlate tightly with GEMS performance across datasets and follow a calibrated envelope of complex-wise prediction errors, enabling a priori risk estimates for downstream models.

Beyond scalar likelihoods, we show that trajectory-level statistics of the PF-ODE, capturing path geometry, stiffness, vector-field spikiness, energetic cost, and drift smoothness—carry complementary OOD information. A simple density-ratio classifier in this feature space outperforms strong non-diffusion baselines built on GEMS embeddings and adaptive uncertainty (Rate-In), despite never using binding-affinity labels.

This trajectory-aware OOD detection approach can offer a computational advantage: Given a diffusion model trained on the training distribution, trajectory features are fast to obtain and can potentially replace slower and more computationally intensive deterministic methods of OOD quantification (such as those described above), especially in settings where new data appears frequently and OOD assessment must be performed rapidly. Moreover, for other irregular graph data, robust complementary methods for deterministic OOD quantification may not exist. In these cases, likelihoods assigned by a diffusion model might be the only viable method for estimating a sample’s OOD degree.

Because the framework is fully generative and label-free, it extends beyond protein–ligand complexes to any modality that admits continuous diffusion, offering a general recipe for OOD quantification and error forecasting in geometric deep learning.

4 Discussion

This work aims to contribute meaningfully to the debate between generalization and memorization of machine learning models. While new models frequently report strong generalization, such claims are often accompanied by concerns that performance may largely stem from memorizing recurring patterns shared between training and test data. This concern is particularly relevant for models trained on complex data such as protein-ligand interactions, where structural homologies are non-trivial to detect and identical interaction patterns can occur in otherwise dissimilar complexes. We argue that potential data leakage and distributional overlap should be analyzed at the level of the data representation accessible to the model, rather than at the raw structural data. This way can we rigorously evaluate whether training and test samples share similar representations for the model to exploit.

By explicitly relating prediction errors to OOD scores, we can disentangle generalization from dataset-specific memorization. The steepness of the increase in prediction errors with higher log-likelihood can serve as a quantitative marker of generalization ability. The rate at which prediction errors increases as a function of the log-likelihood can serve as a quantitative proxy for generalization capability. A steep increase implies that model performance relies on distributional overlap, degrading rapidly for OOD data. Conversely, a shallow increase indicates robust generalization, demonstrating the model’s resilience in regions of chemical and structural space that are less-represented within its training data. This enables direct comparisons across competing models, moving beyond single benchmark values. In this sense, OOD quantification can act as a certificate for benchmark datasets. Comparing the distribution of OOD log-likelihoods with respect to the training data clarifies whether high benchmark performance reflects actual generalization or mere memorization.

We emphasize that our method should be read as one concrete instantiation of a broader and robust *OOD detection blueprint*. The core requirement is simply a generative dynamical model—a diffusion or flow-matching model—trained to represent the in-distribution of irregular graphs. Once such a model is available, the induced probability-flow dynamics provide a natural coordinate system in which to build *trajectory-level diagnostics*: one can design score functions and summary statistics that probe whichever structural regularities are relevant for the application, and then detect OOD by identifying trajectories whose behavior is atypical under the training distribution.

For instance, in protein-ligand settings one can augment likelihoods with diffusion-time features that explicitly track (i) *geometric stability* (e.g. preservation of pocket shape, RMSD-like drift of key residues, local rigidity/strain, or deviations from expected bond-length/angle priors after bond inference), (ii) *interaction physics* (e.g. evolution of hydrogen-bond patterns, salt-bridge and π -stacking persistence, steric clashes, packing density, solvent-exposed surface area proxies, or Coulomb/Lennard-Jones-style surrogate energies computed from coordinates), and (iii) *biological coupling signals* (e.g. co-folding/co-adaptation descriptors such as correlated motions of residue substructures with ligand substructures, contact-map consistency over diffusion time, or stability of secondary-structure-like local motifs in the pocket neighborhood). More broadly, any measurable property of the evolving state—including constraints, symmetries, conservation-like quantities, or domain-specific interaction scores—can be turned into a trajectory statistic and combined into a multivariate typicality model, yielding an OOD detector tailored to the scientific failure modes of interest.

While this work provides a proof of concept demonstrating that diffusion PF-ODE trajectory features enable successful OOD quantification, significant potential remains to improve the diffusion model’s sensitivity to chemical differences between ligands. Among the nine datasets tested, we identified one OOD dataset of metalloenzymes (carbonic anhydrases) that the model consistently flagged as in-distribution. We hypothesize that the current model struggles to recognize unique chemistry embedded in common scaffold structures. While the ligands in these complexes possessed simple, common scaffold structures, they were characterized by high sulfur content and the presence of sulfonamide groups interacting with a zinc ion. This kind of chemistry is highly underrepresented in the dataset. Future work should focus on improving the model’s chemical understanding to better capture such distinct chemistry within otherwise familiar geometries.

5 Method

5.1 Datasets

Existing diffusion models for protein–ligand interactions such as DiffSBDD [11] and TargetDiff [12] were trained on datasets of experimental structures extracted from the Protein Data Bank (PDB), frequently augmented with artificial complexes generated by docking tools [13]. The PDBbind database (v.2020) represents the subset of all available experimental protein-ligand complex structures for which binding affinity labels are available [1, 2]. This dataset (N=19’443) served as the main data resource to train and evaluate models in this work.

To evaluate the OOD detection capability of our diffusion model, we split the PDBbind dataset into a training set and several test sets with varying biological uniqueness using PLINDER’s pocket-level clustering based on Local Distance Difference Test IDDT (cluster type *pocket lddt 50 community*) [14]. Seven proteins were selected to represent diverse protein families (PDB IDs: 1nvq, 1sqa, 2p15, 2vw5, 3dd0, 3f3e, 3o9i). For each representative protein, all complexes from its cluster were assigned to a separate test set, thereby removing entire protein families from the training dataset. To be able to use the CASF2016 benchmark [6] as an additional test dataset, we applied CleanSplit filtering [3] to the training data to remove similarities with CASF2016. We then further split the training data randomly into final training and validation set using a ratio of 90/10. This process resulted in the following datasets:

- Training dataset (N=10’510): Dataset containing 90% of the remaining complexes after OOD dataset extraction and CleanSplit filtering.
- Validation dataset (N=1167): Dataset containing 10% of the remaining complexes after OOD dataset extraction and CleanSplit filtering.
- CASF2016 benchmark (N=285): Diverse dataset with protein-ligand complexes from 57 different protein families. Data leakage reduced through CleanSplit filtering.
- 1nvq OOD (N=2714): Cluster of serine/threonine-protein kinase binding pockets
- 1sqa OOD (N=736): Cluster of Urokinase-type plasminogen activator pockets
- 2p15 OOD (N=462): Cluster of estrogen receptor binding pockets
- 2vw5 OOD (N=207): Cluster of molecular chaperone HSP82 binding pockets
- 3dd0 OOD (N=475): Cluster of carbonic anhydrase binding pockets
- 3f3e OOD (N=391): Cluster of transporter protein binding pockets
- 3o9i OOD (N=469): Cluster of HIV-1 protease binding pockets

This dataset split was employed for both the diffusion model and the GEMS binding affinity prediction model. The diffusion model was trained on the training dataset. Validation losses were computed throughout the training process using the validation dataset. All non-training datasets (validation, CASF2016, and OOD sets) were subsequently used to evaluate the model’s ability to differentiate and rank datasets according to their OOD level relative to the training data. GEMS was trained exclusively on the training dataset using 5-fold cross-validation (CV). All other datasets served as test sets to evaluate generalization capability to datasets of varying distribution shifts, ranging from IID (e.g. the validation set) to highly OOD (e.g. the HIV proteases).

5.2 Diffusion Model

Our diffusion model reuses only the EGNN backbone architecture from DiffSBDD [11]; all other components, ranging from the diffusion training infrastructure, to metrics and evaluation components and sampling procedures (covering also the PF-ODE implementation) are specific to this work.

5.2.1 Background and Motivation

Continuous diffusion and probability-flow. Diffusion models specify a family of corrupted observations $\{\mathbf{x}_t\}_{t \in [0,1]}$ linked by a forward SDE (typical setup of [15])

$$d\mathbf{x} = f(\mathbf{x}, t) dt + g(t) d\mathbf{w}, \quad \mathbf{w} \text{ a standard Wiener process,} \quad (5.1)$$

and learn a time-indexed score field $s(\mathbf{x}, t) = \nabla_{\mathbf{x}} \log p_t(\mathbf{x})$ to reverse the corruption. Under mild regularity, the *probability-flow ODE* (PF-ODE) $\dot{\mathbf{x}} = \tilde{f}(\mathbf{x}, t)$ transports samples deterministically while matching the SDE marginals at every t ; its drift is a functional of the score. For variance-exploding (VE) designs with $f \equiv 0$ and scalar noise scale $\sigma(t)$, the conditional $p(\mathbf{x}_t | \mathbf{x}_0) = \mathcal{N}(\mathbf{x}_0, \sigma(t)^2 I)$ and the PF-ODE drift is proportional to the score,

$$\dot{\mathbf{x}}(t) = -\frac{1}{2}g(t)^2 s(\mathbf{x}_t, t), \quad (5.2)$$

yielding an exact change-of-variables likelihood for any clean input \mathbf{x}_0 ,

$$\log p(\mathbf{x}_0) = \log p_1(\mathbf{x}_1) + \int_0^1 \text{tr} \left(\frac{\partial \tilde{f}}{\partial \mathbf{x}}(\mathbf{x}(t), t) \right) dt, \quad (5.3)$$

where $\mathbf{x}(1)$ is the terminal state and p_1 is the induced terminal density (Gaussian in the VE case). Equation (5.3) shows that diffusion models are not only samplers but also differentiable density models once a numerically stable divergence estimator is in place.

Denoising as deconvolution (posterior mean). In the VE setting, corruption is a Gaussian convolution $\mathbf{x}_t = \mathbf{x}_0 + \sigma(t)\epsilon$ with $\epsilon \sim \mathcal{N}(0, I)$. Recovering \mathbf{x}_0 from \mathbf{x}_t is a classical *deconvolution* problem whose Bayes estimator under squared loss is the posterior mean:

$$\hat{\mathbf{x}}_0(\mathbf{x}_t, t) = \mathbb{E}[\mathbf{x}_0 | \mathbf{x}_t, t] = \arg \min_{\mathbf{y}} \mathbb{E}[\|\mathbf{y} - \mathbf{x}_0\|_2^2 | \mathbf{x}_t, t]. \quad (5.4)$$

The conditional score is *affine* in \mathbf{x}_0 ,

$$s(\mathbf{x}_t, t | \mathbf{x}_0) = \frac{\mathbf{x}_0 - \mathbf{x}_t}{\sigma(t)^2}, \quad (5.5)$$

so taking expectation over $p(\mathbf{x}_0 | \mathbf{x}_t, t)$ gives

$$\hat{s}(\mathbf{x}_t, t) = \mathbb{E}[s(\mathbf{x}_t, t | \mathbf{x}_0) | \mathbf{x}_t, t] = \frac{\hat{\mathbf{x}}_0(\mathbf{x}_t, t) - \mathbf{x}_t}{\sigma(t)^2}. \quad (5.6)$$

Thus, learning any mechanism that reliably produces the posterior mean clean signal *directly delivers* the score needed for both sampling and PF-ODE likelihoods.

5.2.2 Unified continuous diffusion for molecular coordinates and identities

Contribution We introduce a unified *continuous* diffusion model for molecules that treats both 3D geometry and discrete chemical identities in a single Euclidean state: we learn L2-normalized prototypes for the categorical alphabet and run the same VE diffusion on the concatenated coordinates || embeddings, converting class logits to scores via *posterior-mean interpolation*. This yields a single, end-to-end objective and avoids the collapse pathologies of direct score regression on the categorical channel.

Background: score interpolation for categorical data. Under VE corruption $\mathbf{x}_t = \mathbf{x}_0 + \sigma(t)\epsilon$ with $\epsilon \sim \mathcal{N}(0, \mathbf{I})$, the conditional score is an affine function of the posterior mean of the clean variable:

$$s(\mathbf{x}_t, t) = \frac{\mathbb{E}[\mathbf{x}_0 | \mathbf{x}_t, t] - \mathbf{x}_t}{\sigma(t)^2}. \quad (5.7)$$

For a categorical variable represented by L2-normalized prototypes $\mathbf{e}_1, \dots, \mathbf{e}_V \in \mathbb{R}^d$ and a noisy embedding \mathbf{x}_t , if a denoiser outputs logits \mathbf{z} with class posteriors $p(i | \mathbf{x}_t, t) = \text{softmax}(\mathbf{z})_i$, then the posterior mean over the clean embedding is the finite mixture

$$\hat{\mathbf{e}}_0(\mathbf{x}_t, t) = \sum_{i=1}^V p(i | \mathbf{x}_t, t) \mathbf{e}_i, \quad (5.8)$$

and the corresponding *interpolated score* for the categorical block follows by plugging (5.8) into (5.7):

$$\hat{s}(\mathbf{x}_t, t) = \frac{\hat{\mathbf{e}}_0(\mathbf{x}_t, t) - \mathbf{x}_t}{\sigma(t)^2}. \quad (5.9)$$

This ‘‘score via posterior mean’’ viewpoint enables standard cross-entropy training on logits while keeping the dynamics continuous in time and space (cf. CDCD, [16]).

Learning molecular embeddings without collapse. Direct score matching on the categorical prototypes is ill-posed: with Gaussian corruption around each prototype, a degenerate joint optimum collapses all $\{\mathbf{e}_i\}$ to a single point, making the noise perfectly predictable while erasing identity. We therefore *train the categorical path with cross-entropy on logits and derive the score via (5.8)–(5.9)*. Concretely, let $y \in \{1, \dots, V\}$ be the clean token with prototype \mathbf{e}_y , sample $t \sim p(t)$ and $\epsilon \sim \mathcal{N}(0, \mathbf{I})$, and form the noisy embedding

$$\mathbf{x}_t = \mathbf{e}_y + \sigma(t) \epsilon.$$

The denoiser produces a normalized feature $\hat{\mathbf{h}}_\theta(\mathbf{x}_t, t) \in \mathbb{R}^d$ and cosine logits

$$z_i(\mathbf{x}_t, t) = \kappa(t) \langle \mathbf{e}_i, \hat{\mathbf{h}}_\theta(\mathbf{x}_t, t) \rangle, \quad \|\mathbf{e}_i\|_2 = \|\hat{\mathbf{h}}_\theta\|_2 = 1, \quad (5.10)$$

with either a *theory-aligned* temperature $\kappa(t) = \sigma(t)^{-2}$ (matching the Bayes posterior for unit-norm prototypes) or a fixed $\kappa=1$ for simplicity.¹ Our primary loss is standard hard-label cross-entropy

$$\mathcal{L}_{\text{cat}}(\theta, \{\mathbf{e}_i\}) = \mathbb{E}_{y,t,\epsilon} \left[-\log \text{softmax}(\mathbf{z}(\mathbf{x}_t, t))_y \right], \quad (5.11)$$

which learns posteriors $p_\theta(i | \mathbf{x}_t, t) = \text{softmax}(\mathbf{z})_i$ and, through (5.8)–(5.9), yields the interpolation-derived categorical score.

These cosine logits remove scale indeterminacy (no norm inflation), enlarge inter-class margins on the sphere, and stabilize the interpolation-derived score, yielding a compact, regularizer-free recipe for joint training of coordinates and identities.

Unified diffusion over coordinates || embeddings. We concatenate continuous 3D coordinates with the learned categorical embeddings and run the same VE diffusion across the entire state. This brings three concrete advantages: (i) *Principled estimator*. Denoising is deconvolution: coordinates are regressed to their clean values; categorical embeddings use the exact finite average (5.8). The resulting score (5.9) is consistent by construction. (ii) *Numerical stability*. Cross-entropy over a small chemical alphabet (tens of atom/residue types) is well-conditioned and avoids the small- σ gradient blow-ups that can afflict direct score regression; L2 normalization bounds activations and improves Lipschitz behavior across noise scales. (iii) *Exact finite averaging*. Unlike language modeling, V here is small, so (5.8) is computed *exactly* at every node and time step—preserving chemical similarity (nearby classes \Rightarrow nearby embeddings) while representing genuine superpositions at intermediate noise levels.

Geometry and symmetry. Molecular validity depends on geometry and symmetry. Our diffusion state always enforces translation invariance by projecting the coordinate block to the center-of-mass (COM)-free subspace per complex; the same projection is applied to all coordinate noise, drifts, and divergence probes. An SE(3)-equivariant graph denoiser updates coordinates and predicts logits conditioned on noisy coordinates || embeddings, allowing geometric cues to inform identity and vice versa. Because (5.9) expresses the PF-ODE drift through posterior means, the same denoiser underpins both generation and likelihood evaluation without changing objective or architecture.

¹We enforce the unit-sphere constraints by projection after each update: $\mathbf{e}_i \leftarrow \mathbf{e}_i / \|\mathbf{e}_i\|_2$ and $\hat{\mathbf{h}}_\theta \leftarrow \mathbf{h}_\theta / \|\mathbf{h}_\theta\|_2$.

Consequence for likelihoods and OOD. Unifying geometry and identity within a continuous diffusion equipped with exact posterior-mean interpolation yields a *single*, self-consistent PF-ODE whose pathwise divergence and terminal Gaussian define a tractable, per-complex log-likelihood via (5.3). Likelihoods accumulate information across a continuum of noise scales, furnishing a sensitive typicality score for out-of-distribution detection in molecular settings where categorical spaces are small and geometric constraints are paramount.

5.2.3 Diffusion Model Setup

State, symmetries, and encoders Protein-ligand complexes were mapped to fully-connected graphs including ligand atoms and C α atoms of all amino acids with atoms less than 5 Å from any ligand atom. We represent a batched complex by nodes $i = 1, \dots, N$ with coordinates $\mathbf{r}_i \in \mathbb{R}^3$ and categorical labels $y_i \in \{1, \dots, V\}$ representing atom/residue types. Edge features were initialized as the Euclidean distance between the connected nodes. Two learnable encoders map atom/residue types to L2-normalized embeddings $\mathbf{e}_{y_i} \in \mathbb{R}^d$, and we define the per-node state $\mathbf{x}_i = [\mathbf{r}_i \parallel \mathbf{e}_{y_i}] \in \mathbb{R}^{3+d}$. For each complex in the batch we remove global translation by projecting the coordinate block to the center-of-mass (COM)-free subspace at every step; the same projection is applied to all coordinate noise and updates. This enforces translation invariance and reduces the effective coordinate degrees of freedom.

Noise schedule and preconditioning We use a monotone VE schedule $\sigma : [0, 1] \rightarrow (\sigma_{\min}, \sigma_{\max}]$; in practice we parameterize σ so that $\log \sigma$ is approximately linear in t and is easily invertible for sampler step allocation. Following EDM-style preconditioning, inputs are scaled by $c_{\text{in}}(t) = (\sigma(t)^2 + \sigma_{\text{data}}^2)^{-1/2}$ and outputs by $c_{\text{out}}(t) = \sigma(t)\sigma_{\text{data}}(\sigma(t)^2 + \sigma_{\text{data}}^2)^{-1/2}$ to equalize dynamic range across noise levels.

Equivariant denoiser The denoiser is an EGNN that consumes the concatenated state with a scalar noise/time conditioning and returns two heads per node: a clean coordinate estimate $\hat{\mathbf{r}}_{0,i}$ and logits $\mathbf{z}_i \in \mathbb{R}^V$. Using \mathbf{z}_i we form probabilities $p_i = \text{softmax}(\mathbf{z}_i)$ and the posterior-mean clean embedding

$$\hat{\mathbf{e}}_{0,i} = \sum_{k=1}^V p_i(k) \mathbf{e}_k. \quad (5.12)$$

Collecting per-node predictions, the denoiser yields $\hat{\mathbf{x}}_0 = [\hat{\mathbf{r}}_0 \parallel \hat{\mathbf{e}}_0]$.

Training objective At a sampled noise level t we construct noisy inputs $\mathbf{x}_t = \mathbf{x}_0 + \sigma(t)\epsilon$ with $\epsilon \sim \mathcal{N}(0, I)$, enforcing COM-free noise in the coordinate block. The loss combines a coordinate regression term with a categorical cross-entropy:

$$\mathcal{L} = \lambda_{\text{coord}} \mathbb{E}[w(t) \|\hat{\mathbf{r}}_0 - \mathbf{r}_0\|_2^2] + \lambda_{\text{CE}} \mathbb{E}\left[\sum_{i=1}^N \text{CE}(\mathbf{z}_i, y_i)\right] + \lambda_{\text{geom}} \mathcal{L}_{\text{geom}}, \quad (5.13)$$

where $w(t)$ is the EDM weight that flattens the effective noise-level distribution, and $\mathcal{L}_{\text{geom}}$ optionally encodes geometric regularizers (e.g., connectivity, radius of gyration, cycle incentives). L2 normalization of the embedding tables stabilizes learning and empirically prevents collapse without additional penalties.

Reverse-time sampling Sampling follows the reverse SDE with Euler–Maruyama integration coupled with COM projection after each step. The drift uses the denoiser’s effective clean prediction and the schedule derivatives (computed by automatic differentiation on σ). This produces coordinate trajectories and categorical superpositions that resolve as noise decays.

Probability–flow ODE and likelihood For the PF-ODE, we use the VE correspondence that yields a drift proportional to the interpolated score. In particular, with (5.7)–(5.9) and the standard VE choice $g(t) = \sqrt{2} \sigma'(t)$ one obtains

$$\dot{\mathbf{x}}(t) = -\frac{1}{2}g(t)^2 \hat{s}(\mathbf{x}_t, t) = \alpha(t) (\mathbf{x}_t - \hat{\mathbf{x}}_0(\mathbf{x}_t, t)), \quad \alpha(t) := \frac{g(t)^2}{2\sigma(t)^2}, \quad (5.14)$$

where $\hat{\mathbf{x}}_0$ uses the coordinate head and the class-probability-weighted mean embedding. We integrate (5.14) forward from $t=0$ (clean) to $t=1$ (noisy) with Heun’s method in the COM-free subspace. The log-density is then computed by (5.3). The terminal density $p_1(\mathbf{x}_1)$ factors over nodes and splits into a coordinate block and an embedding block. In the coordinate block, the COM constraint reduces the degrees of freedom of a complex with n atoms by 3 (in 3D), leading to

$$\log p_{1,\text{coord}} = -\frac{1}{2\sigma(1)^2} \|\mathbf{r}_1\|_2^2 - \frac{(3n-3)}{2} \log(2\pi\sigma(1)^2), \quad (5.15)$$

while the embedding block is isotropic Gaussian in \mathbb{R}^d per node (with d the embedding dimension). Summing the two yields $\log p_1(\mathbf{x}_1)$.

Divergence via Hutchinson under COM constraints. We estimate the divergence in (5.3) with a Hutchinson trace estimator. Let $\epsilon \sim \mathcal{N}(0, I)$ be a probe in the joint state; project its coordinate block to the COM-free subspace to match the dynamics. A single vector–Jacobian product computes $\epsilon^\top \nabla_{\mathbf{x}} \tilde{f}(\mathbf{x}, t)$, and averaging a few probes per time step produces a low-variance estimate. To ensure consistency, the denoiser and schedule are evaluated with gradients enabled along the PF-ODE path, and COM projection is applied to *both* drifts and probes.

Algorithm 1 Training (embedding diffusion with cross-entropy)

Require: dataset $\{\mathbf{r}_0, y\}$, encoders Enc, schedule $\sigma(t)$, EGNN denoiser D

- 1: **while** not converged **do**
 - 2: sample minibatch; form embeddings $\mathbf{e}_0 \leftarrow \text{Enc}(y)$ (L2-normalize)
 - 3: COM-center coordinates; sample $t \sim p(t)$; set $\mathbf{x}_0 \leftarrow [\mathbf{r}_0 \| \mathbf{e}_0]$
 - 4: sample $\epsilon \sim \mathcal{N}(0, I)$, make coordinate block COM-free; set $\mathbf{x}_t \leftarrow \mathbf{x}_0 + \sigma(t)\epsilon$
 - 5: $(\hat{\mathbf{r}}_0, \mathbf{z}) \leftarrow D(\mathbf{x}_t, t)$; $\hat{\mathbf{e}}_0 \leftarrow \sum_i \text{softmax}(\mathbf{z})_i \mathbf{e}_i$
 - 6: compute \mathcal{L} via (5.13); update parameters
 - 7: **end while**
-

Algorithm 2 PF-ODE likelihood per complex

Require: clean state \mathbf{x}_0 , schedule σ , denoiser D , time grid $0 = t_0 < \dots < t_T = 1$

- 1: COM-center coordinates in \mathbf{x}_0 ; set $\ell \leftarrow 0$, $\mathbf{x} \leftarrow \mathbf{x}_0$
 - 2: **for** $k = 0, \dots, T-1$ **do**
 - 3: $\hat{\mathbf{x}}_0 \leftarrow$ posterior mean from $D(\mathbf{x}, t_k)$
 - 4: $\tilde{f} \leftarrow \alpha(t_k)(\mathbf{x} - \hat{\mathbf{x}}_0)$ (COM-free)
 - 5: sample m Hutchinson probes $\epsilon^{(j)}$; project coordinate blocks to COM-free
 - 6: $\widehat{\text{div}} \leftarrow \frac{1}{m} \sum_j \epsilon^{(j)\top} \nabla_{\mathbf{x}} \tilde{f}(\mathbf{x}, t_k)$
 - 7: $\ell \leftarrow \ell + \widehat{\text{div}}(t_{k+1} - t_k)$
 - 8: Heun step: predictor $\mathbf{x}' = \mathbf{x} + \tilde{f} \Delta t$; corrector with \tilde{f}' at t_{k+1}
 - 9: COM-center coordinates of the updated state
 - 10: **end for**
 - 11: compute $\log p_1(\mathbf{x})$ with DOF correction; **return** $\log p_1(\mathbf{x}) + \ell$
-

5.2.4 Diffusion Model Training and Evaluation

Data Preparation To prepare the protein-ligand complex structures for diffusion model training and evaluation, all complexes underwent a standardized preprocessing. Structural files for proteins

(PDB) and ligands (SDF) were parsed using Gemmi (v.0.7.0) and processed using Numpy (v.1.26.4), PyTorch (v.2.7.0) and PyTorch Geometric (v.2.6.1).

Ligand atom coordinates and types were extracted from the Gemmi objects (hydrogens omitted). Ligand atom coordinates were combined into a ligand feature matrix (\mathbf{C}_L) and ligand atom types were one-hot-encoded to construct the ligand feature matrix (\mathbf{F}_L) using the following 10 categories:

- C, N, O, S, B, Br, Cl, P, I, F

For each residue in the protein, the pairwise distances between the residue’s atoms and all ligand atoms were computed. A protein residue was designated as a pocket residue if any of its atoms were within 5Å of a ligand atom. The C-alpha (C_α) coordinates of all identified pocket residues were combined to form the protein coordinate matrix (\mathbf{C}_P). The corresponding residue type 3-letter-codes were standardized and one-hot-encoded to create the protein feature matrix (\mathbf{F}_P), using the following 21 categories (with metal ions aggregated into a single group):

- ALA, CYS, ASP, GLU, PHE, GLY, HIS, ILE, LYS, LEU, MET, ASN, PRO, GLN, ARG, SER, THR, VAL, TRP, TYR, METAL

In summary, four arrays were computed to represent a complex:

$$\begin{aligned} \text{Ligand coordinates: } & \mathbf{C}_L \in \mathbb{R}^{N_L \times 3} \\ \text{Protein coordinates: } & \mathbf{C}_P \in \mathbb{R}^{N_P \times 3} \\ \text{Ligand features: } & \mathbf{F}_L \in \mathbb{R}^{N_L \times 10} \\ \text{Protein features: } & \mathbf{F}_P \in \mathbb{R}^{N_P \times 21} \end{aligned}$$

where N_L is the number of ligand atoms and N_P is the number of pocket residues. These four arrays were then combined in a PyTorch Geometric Data object for each complex. To construct datasets, these Data objects were combined into PyTorch datasets according to the splitting outlined in section 5.1.

Training and Hyperparameter Optimization To maximize the model’s performance and ensure robust training, we performed a systematic hyperparameter optimization. The search space was defined across several key architectural and training features, including learning rate, the number of sampling steps, the number of EGNN layers, the joint and hidden embedding sizes and the edge feature dimensionality. Initially, we employed a randomized search with short training runs to set reasonable search space boundaries. Then we explored the resulting search space outlined in Table 3 using Bayesian optimization with the Optuna (v.4.4.0) python package. The best parameter combination was selected based on a joint assessment of validation loss and sampling-based evaluations, including percent of fragmented ligands, mean number of ligand fragments, mean number of rings, mean ring size and Jensen-Shannon divergences between training and sampling ligand atom and protein residue type distributions. The model was trained using the final configuration (in the rightmost column of the Table 3), resulting in a model with with 6’386’128 parameters. The training process was continued for as long as the training and validation losses continued to decrease, but was stopped eventually after 1400 epochs. The last saved model (epoch 1390) was used for log-likelihood based OOD evaluation. Protein-ligand interactions sampled from this model contained ligands with 92% chemical validity, 72% of unfragmented ligands and a mean number of 2.34 rings with mean size of 5.31 per molecule. Divergences in atom and amino acid type distributions (Jensen-Shannon) from the training data were very low, at 0.0017 and 0.004, respectively.

5.3 GEMS Training and Evaluation

The Graph Neural Network (GNN) for efficient molecular scoring (GEMS) binding affinity prediction model [3] was trained using the same dataset splits as the diffusion model, following the authors’ original instructions.

Table 3: Hyperparameter search spaces and selected optimal values.

Parameter	Search Space	Selected
num_sampling_steps	{50, 100, 200, 300, 400}	400
joint_nf	{32, 64, 128, 256}	256
hidden_nf	{64, 128, 256}	256
n_layers	{4, 6, 8}	6
edge_embedding_dim	{8, 16, 32, 64}	64
learning_rate	$\{5 \times 10^{-5}, 1 \times 10^{-4}, 5 \times 10^{-4}, 1 \times 10^{-3}, 5 \times 10^{-3}\}$	1×10^{-4}
batch_size	{16, 32, 64, 128}	16

Data Preparation and Training Custom datasets were constructed for the training, validation, CASF2016, and OOD sets. This involved computing graph representations of the complexes across the entire PDBbind v.2020 dataset, featurized using language model embeddings derived from ESM2 [17], Ankh [18], and ChemBERTa2 [19].

The GEMS model was trained on the training dataset using 5-fold cross-validation (CV) and the default hyperparameters:

- Loss Function: Root Mean Squared Error (RMSELoss)
- Optimizer: Stochastic Gradient Descent (SGD)
- Batch Size: 256
- Learning Rate: 0.001 (constant)
- Weight Decay: 0.001

The model was trained using early stopping, terminating the process when the validation RMSE did not decrease for 100 epochs.

Model Selection and Evaluation We performed a hyperparameter search on the dropout rate applied before the final regression head. The model with a dropout rate of 0.6 was selected, as it showed the lowest and most consistent validation loss across all five folds of the cross-validation. To evaluate performance on the validation, CASF2016, and OOD datasets, the predictions from the five models generated during the 5-fold CV were averaged to create an ensemble prediction.

Evaluation Metrics The coefficient of determination (R^2) was chosen as the main readout for model performance. Other common regression metrics, such as the Pearson Correlation Coefficient (PCC) and Root Mean Squared Error (RMSE), were disregarded due to specific limitations. PCC is insensitive to scale offsets, meaning a high correlation score can coexist with large absolute errors. Conversely, prediction RMSE values are sensitive to variations in the label scale and variance across different datasets, distorting performance comparisons. For datasets with a narrow label distribution, naive models (which predict the dataset mean for all complexes) can achieve deceptively low RMSE values, whereas the same naive models would achieve poor RMSE on datasets with a wide label distribution. R^2 normalizes performance relative to the target variance, providing a fairer comparison across diverse datasets. To compute complex-wise errors, we applied a similar normalization to account for varying label spread across datasets. Specifically, we used Variance-Normalized Errors (VNE), calculated by dividing the absolute error of each prediction by the variance of the dataset’s labels. This effectively rescales the error relative to the difficulty of the dataset, providing a metric that reflects how the model improves sample scoring over a naive baseline that simply predicts the dataset mean.

5.4 Protein-Ligand Complex Similarity Computation

To compute a similarity score between two protein-ligand complexes, Tanimoto ligand similarity, protein similarity (TM scores), and a pocket-aligned ligand root-mean-square-deviation were combined into an

overall structure-based similarity score. This combination captures the presence of similar interaction patterns between two protein-ligand complexes on a structural level. These similarity scores were precomputed in our earlier work [3] and were reused here:

- The Tanimoto similarity score to compare ligand structure was computed using RDKit library v.2024.03.3 based on count-based molecular fingerprints (GetCountFingerprint) of size 2048 and radius 2.
- TM-align [8] was used to assess protein structural similarity and to align complexes based on their protein residues. This algorithm identifies the best structural alignment between protein pairs, using a scoring function based on the RMSD of aligned residues and a length normalization factor, making it useful for identifying structural similarities regardless of sequence similarity. To find if one of the proteins is well represented within the other, we considered TM-scores normalized by the lengths of both amino acid chains and used the highest result.
- A root-mean-square-deviation (RMSD) is computed to compare ligand positioning in the binding pocket of the proteins. For this, the protein structures were aligned together with the bound ligands by applying the translation vector and rotation matrix that TM-align used to generate an optimal protein alignment. Then, the atom coordinates of the aligned ligands were compared by computing the RMSD between the nearest points in the two point clouds. In case of different atom counts, the distances from each atom in the larger ligand to its nearest neighbor in the smaller ligand, resulting in larger RMSD values for ligands with different atom counts.

To aggregate these similarity scores into an simple aggregate score representing similarity on the protein-ligand interaction level, we defined

$$S = \max \{ T_{\text{Tanimoto}} + T_{\text{TM-score}} + (1 - \text{RMSD}), 0 \}.$$

Complex pairs possessing an identical pocket, identical ligands, and matching ligand binding pose achieve the maximum score of 3.0. This score is primarily suited for our use case of detecting and comparing highly similar complexes and is robust in that range. However, its robustness decreases when comparing and ranking complexes in low-level similarity ranges, which is not relevant to our current analysis goals.

5.5 Trajectory-aware out-of-distribution detection

The PF-ODE in (5.3) yields a scalar log-likelihood $\ell(x)$ and, along the same forward integration, a set of trajectory summaries that quantify how the flow behaves on the way from clean to noise. We detect OOD samples by embedding these *PF-ODE features* into a low-dimensional space and fitting separate density models for in-distribution (ID) and OOD trajectories. At test time we use a log-density ratio between the ID and OOD models as a trajectory-aware OOD score.

Feature construction. We aggregate $d=19$ PF-ODE trajectory statistics per complex (full list in Fig. S2). For exposition we display only the most discriminative coordinates:

$$\phi(x) = \left[\begin{array}{l} \ell(x), \text{ path tortuosity, path efficiency,} \\ \text{max Lipschitz, VF spikiness, mean acceleration,} \\ \text{total flow energy, VF } \ell_2 \text{ mean, coord-feature coupling, ...} \end{array} \right].$$

In practice, we apply a train-only preprocessing pipeline (quantile transform, standardization, and PCA) to the full 19-dimensional feature vector and retain the top m principal components (with $m=15$ in our experiments).

Interpretation The selected statistics describe how hard the flow works and how steadily it does so. Paths that wander—summarized by tortuosity and its inverse, efficiency—indicate geometric inefficiency that is typical under shift. Local Lipschitz estimates read off stiffness: nearby states elicit disproportionately different drifts when the model is acting on OOD data. Field size and burstiness, captured by the vector-field ℓ_2 mean and a spikiness ratio, reveal large corrective pushes that concentrate at intermediate noise scales. Mean acceleration records the lack of temporal smoothness in the drift, while total flow energy, $\sum_t f_t^\top \Delta x_t$, aggregates the directed work along the trajectory. Finally, coord–feature coupling measures how spatial updates co-move with feature updates across atoms and residues.

Empirically these quantities move together under distribution shift: stiffer and burstier fields, higher acceleration, and longer, less efficient paths tend to co-occur, whereas in-distribution trajectories remain shorter, smoother, and energetically modest. This coordinated variation explains their strong loadings on the leading PCA component, yielding a single, high-variance axis along which ID and OOD separate cleanly.

Class-conditional density model. Let \mathcal{I} index ID training samples and \mathcal{O} index OOD calibration samples for a given shift condition, with corresponding PF-ODE features

$$X_{\text{ID}} = \{\phi(x_i)\}_{i \in \mathcal{I}}, \quad X_{\text{OOD}} = \{\phi(x_j)\}_{j \in \mathcal{O}}.$$

We first learn a preprocessing map

$$T = \Pi_m \circ Z \circ Q,$$

where Q is a marginal quantile transform to normal scores (fitted on X_{ID}), Z is standardization (mean/variance estimated from X_{ID}), and Π_m projects onto the top m principal components (PCA fit on X_{ID}). This yields low-dimensional embeddings

$$z_i = T\phi(x_i) \in \mathbb{R}^m, \quad i \in \mathcal{I}, \quad z_j = T\phi(x_j) \in \mathbb{R}^m, \quad j \in \mathcal{O}.$$

In this PC space we fit separate Gaussian KDEs for ID and OOD:

$$\hat{p}_{\text{ID}}(z) = \frac{1}{|X_{\text{ID}}| h_{\text{ID}}^m} \sum_{i \in \mathcal{I}} \frac{1}{(2\pi)^{m/2}} \exp\left(-\frac{1}{2} \left\| \frac{z - z_i}{h_{\text{ID}}} \right\|_2^2\right),$$

$$\hat{p}_{\text{OOD}}(z) = \frac{1}{|X_{\text{OOD}}| h_{\text{OOD}}^m} \sum_{j \in \mathcal{O}} \frac{1}{(2\pi)^{m/2}} \exp\left(-\frac{1}{2} \left\| \frac{z - z_j}{h_{\text{OOD}}} \right\|_2^2\right),$$

with isotropic bandwidths $h_{\text{ID}}, h_{\text{OOD}} > 0$. Each bandwidth is selected by K -fold cross-validation on the corresponding class, maximizing the mean log-likelihood on held-out folds.

Scoring and decision rule (test time). For a test complex x^* we compute $z^* = T\phi(x^*)$ and define the log-density ratio

$$L(x^*) = \log \hat{p}_{\text{ID}}(z^*) - \log \hat{p}_{\text{OOD}}(z^*). \quad (5.16)$$

Large positive values of $L(x^*)$ indicate that the trajectory looks more ID-like than OOD-like, while negative values indicate the opposite. We use the negated ratio

$$S(x^*) = -L(x^*) \quad (5.17)$$

as a continuous OOD score, where larger S means more OOD-like. A binary decision is obtained by thresholding $S(x)$ at a level τ chosen on a labeled calibration set of ID and OOD examples, for example by sweeping τ to optimize a desired trade-off between false positives and true positives. AUROC is reported by sweeping τ over the full range of observed scores, treating OOD as the positive class. Note that

$$L(x) = \log \frac{P_{\text{ID}}(x)}{P_{\text{OOD}}(x)},$$

so $L(x) > 0$ favors the ID hypothesis and $L(x) < 0$ favors the OOD hypothesis. All results reported below are obtained without any additional outlier trimming of either class.

Bootstrap evaluation under class imbalance. For each OOD split we partition ID and OOD complexes into training, validation, and test subsets. The two KDEs and the preprocessing map T are fit on their respective training data, and the decision threshold τ is fixed once by maximizing the F1-score for the OOD class on the validation set. Because the number of ID decoys can be much larger than the number of OOD binders, naive evaluation on the full test pool would overweight specificity. To obtain a balanced and robust estimate, we keep the OOD test set fixed and repeatedly draw balanced ID test subsets of the same size. For each draw we evaluate the classifier, treating OOD as the positive class, and record AUROC, accuracy, precision, recall, F1 and specificity. We finally report, for each dataset, the mean and standard deviation of these metrics over multiple such bootstrap test subsets. All plots use a representative test subset, while the legends and tables display the aggregated mean \pm standard deviation.

Confidence and risk stratification. We obtain a notion of confidence by ranking $S(x)$ against the empirical score distribution on ID calibration data. The percentile rank of $S(x)$ within this reference distribution can be mapped to qualitative risk levels (e.g. Low/Medium/High) via fixed quantile cutoffs, providing a simple way to stratify predictions by trajectory atypicality.

Why trajectory features help. The scalar PF-ODE likelihood $\ell(x)$ already aggregates information across noise scales via the divergence integral in (5.3). Trajectory summaries add complementary signals that are characteristic of OOD behavior: larger and spikier vector fields, higher and less stable local Lipschitz factors, increased acceleration, and longer, less efficient paths between states. Modeling the *joint* behavior of these quantities (including $\ell(x)$) through a class-conditional density ratio in a low-dimensional PC space yields substantially stronger separation than calibrating $\ell(x)$ alone, while remaining simple and data-efficient. This ensemble of features is what allowed us to successfully draw a strong decision boundary between the training data and the α -carbonic anhydrase structures (3dd0) dataset where the likelihood scores did not provide sufficient discriminative signal. We provide further analysis of this special case in Section S1.4.

Empirical performance. Table S3 summarizes the performance of the trajectory-aware LDR classifier across multiple OOD test splits. For each dataset we report the mean \pm standard deviation of AUROC, accuracy, F1, specificity, precision and recall over balanced bootstrap test subsets, with OOD treated as the positive class. Overall, the method achieves high AUROC and strong specificity on most shifts, with some degradation on the most challenging benchmarks.

5.6 Embedding–space baseline on GEMS

Methodology We construct a non–generative baseline that operates directly in the representation space of a pretrained GEMS encoder. For each complex x , we run the encoder R stochastic passes (e.g. dropout, data augmentation) and obtain vectors $\{E_r(x) \in \mathbb{R}^d\}_{r=1}^R$. We then store a single summary embedding

$$\bar{E}(x) := \frac{1}{R} \sum_{r=1}^R E_r(x) \in \mathbb{R}^d,$$

which serves as a fixed descriptor of x in all subsequent experiments. All baselines described below operate only on these precomputed embeddings and never modify or retrain GEMS.

Unsupervised detectors on ID embeddings. Given the ID training set embeddings $\{\bar{E}(x)\}_{x \in \mathcal{D}_{\text{ID}}^{\text{train}}}$, we fit a family of classical one–class / anomaly detectors. Before fitting, we standardize all features with a single affine transform (mean and variance estimated on $\mathcal{D}_{\text{ID}}^{\text{train}}$). Each detector then assigns an anomaly score $S(x)$ to a test embedding, with the convention that larger values indicate evidence for OOD:

1. **Mahalanobis distance.** We estimate an ID mean $\mu \in \mathbb{R}^d$ and a regularized covariance

$$\Sigma = \text{Cov}(\bar{E}(x)) + \lambda I_d, \quad \lambda > 0,$$

and score a point by its Mahalanobis distance

$$S_{\text{mah}}(x) = \sqrt{(\bar{E}(x) - \mu)^\top \Sigma^{-1} (\bar{E}(x) - \mu)}.$$

2. **k-NN distance.** We build a k -nearest-neighbor index over the ID embeddings (Euclidean metric in the standardized space). The score is the mean distance to the k nearest ID neighbors,

$$S_{\text{knn}}(x) = \frac{1}{k} \sum_{i=1}^k \left\| \bar{E}(x) - \bar{E}(x^{(i)}) \right\|_2,$$

where $x^{(i)}$ denotes the i -th nearest ID training complex to x .

3. **Local Outlier Factor (LOF).** We fit a Local Outlier Factor model on the ID embeddings with novelty detection enabled. LOF returns a negative log-density-like score; we negate it so that larger values correspond to more anomalous points:

$$S_{\text{lof}}(x) = -\text{LOF_score}(x).$$

4. **Isolation Forest.** We fit an Isolation Forest on the ID embeddings. The model outputs higher scores for typical points; we again negate these values,

$$S_{\text{if}}(x) = -\text{IF_score}(x),$$

so that higher scores indicate higher isolation (OOD).

5. **One-Class SVM.** Finally, we fit a one-class SVM with an RBF kernel on the ID embeddings. Its decision function is positive for inliers and negative for outliers; we define

$$S_{\text{svm}}(x) = -\text{OCSVM_decision}(x),$$

so that larger values again correspond to stronger OOD evidence.

These five detectors cover distance-based, density-ratio, isolation-based and margin-based paradigms, all applied to the same fixed GEMS representation.

Calibration and decision rules. For each OOD test split, we re-use the same ID training embeddings but construct a small validation set to obtain a decision threshold. Concretely, given ID and OOD embeddings for a particular split, we randomly partition both into validation and test subsets. Each detector S is trained on $\mathcal{D}_{\text{ID}}^{\text{train}}$ only and then evaluated on the validation embeddings:

$$\{S(x)\}_{x \in \mathcal{D}_{\text{ID}}^{\text{val}}}, \quad \{S(x)\}_{x \in \mathcal{D}_{\text{OOD}}^{\text{val}}}.$$

We treat OOD as the positive class and search over a grid of candidate thresholds τ , selecting the one that maximizes the F1 score on this validation set. This yields a single calibrated threshold τ_S per detector and per OOD split, which is *not* adjusted on the test data.

Evaluation protocol. On the test embeddings for a given split, we report both threshold-free and thresholded performance. For AUROC, we use the raw anomaly scores $S(x)$ and treat OOD as the positive class. For calibrated decisions, we predict

$$\hat{y}(x) = \mathbb{I}\{S(x) > \tau_S\}$$

and compute accuracy, precision, recall, F1 and specificity. To reduce variance and to match the protocol used for the trajectory-aware LDR classifier, all metrics are estimated on balanced bootstrap test subsets: in each of B bootstrap rounds we subsample the ID test set to match the size of the OOD test set, evaluate the metrics, and finally report the mean and standard deviation over these B replicates.

We evaluate performance across the same held-out OOD splits used for the trajectory-aware LDR classifier. For each split we train all five detectors (Mahalanobis, k -NN distance, Local Outlier Factor, Isolation Forest, and one-class SVM) on the ID training embeddings, and then *select the best detector per dataset by AUROC*. This gives a generous reference for what can be achieved by post-hoc anomaly detection on a fixed GEMS representation.

Why we emphasize AUROC. In this setting AUROC is a more robust indicator of detector quality than the thresholded metrics. First, AUROC is threshold-free: it depends only on the ranking induced by the anomaly scores and is invariant to the particular decision threshold. In contrast, accuracy, F1, precision, recall and specificity are all evaluated at a *single* threshold that we explicitly tune on a small validation set to maximize F1. This calibration step is useful to obtain a reasonable operating point, but it can inflate F1 and accuracy even for relatively weak detectors, especially on the balanced 50/50 ID/OOD mixtures used in our bootstrap protocol. Secondly, the balanced evaluation itself is convenient for comparison but does not reflect realistic class imbalance where OOD events are rare; under such imbalance, the same threshold would typically yield very different precision and accuracy, while AUROC remains unchanged. For these reasons, when comparing to the trajectory-aware LDR classifier we primarily interpret AUROC as the main measure of intrinsic separability between ID and OOD, and view F1/accuracy as secondary, operating-point-dependent statistics.

Rationale and limitations. This embedding-space baseline assumes that ID complexes occupy a relatively compact region of the GEMS representation space, and that OOD complexes are either geometrically distant from this region (captured by S_{mah} and S_{knn}) or sparsely supported / difficult to fit by standard one-class models (captured by LOF, Isolation Forest and one-class SVM). The approach is entirely post-hoc: it requires no generative training, no access to the PF-ODE dynamics, and can be implemented with off-the-shelf anomaly detection packages given a frozen GEMS encoder. At the same time, it is a purely static snapshot of representation geometry and does not integrate information along noise-time trajectories or exploit intermediate superpositions of identities.

5.7 Rate-In baseline on GEMS

We include Rate-In [10] as a non-diffusion baseline for OOD detection. Rate-In builds on MC dropout [20], but replaces a fixed global dropout rate with *adaptive, per-sample, per-layer* dropout rates chosen to preserve information flow through the network. Intuitively, in-distribution (ID) inputs admit relatively large dropout rates without disrupting the computation, whereas OOD inputs are much more fragile under dropout perturbations. Rate-In turns this robustness gap into an OOD signal.

Information-preserving dropout. Consider a network with L dropout layers and layer- ℓ activations $h_{\text{in}}^{(\ell)}$ and $h_{\text{out}}^{(\ell)}$. For a given input x and dropout rate p_ℓ at layer ℓ , Rate-In measures how much information about $h_{\text{in}}^{(\ell)}$ survives through dropout by approximating the mutual information

$$I_\ell(p_\ell) \approx I(h_{\text{in}}^{(\ell)}; h_{\text{out}}^{(\ell)} | p_\ell).$$

The “no-dropout” reference

$$I_{\text{full}}^{(\ell)} := I(h_{\text{in}}^{(\ell)}; h_{\text{out}}^{(\ell)} | p_\ell = 0)$$

is computed once per input. The relative information loss at layer ℓ is

$$\delta I_\ell(p_\ell) = \frac{I_{\text{full}}^{(\ell)} - I_\ell(p_\ell)}{I_{\text{full}}^{(\ell)}}.$$

Rate-In chooses the largest dropout rate p_ℓ^* for which $\delta I_\ell(p_\ell)$ stays below a target threshold ϵ (we use $\epsilon = 0.1$ in all experiments).

We approximate

$$I(X; Y) \approx -\frac{1}{2} \log(1 - \rho^2),$$

where ρ is the Pearson correlation between flattened X and Y . To reduce variance, we average over $K = 5$ forward passes with independent dropout masks at the current p_ℓ .

Per-layer rate optimisation. For each input x and each dropout layer ℓ , we solve for p_ℓ^* with a simple multiplicative update:

1. Compute $I_{\text{full}}^{(\ell)}$ with dropout disabled at layer ℓ .
2. Initialise p_ℓ (we use $p_\ell = 0.3$).
3. Repeat for up to $N_{\text{max}} = 20$ iterations:
 - (a) Enable dropout only at layer ℓ with rate p_ℓ , run K stochastic forward passes, and estimate $I_\ell(p_\ell)$ by averaging the MI over these passes.
 - (b) Compute $\delta I_\ell(p_\ell)$.
 - (c) If $|\delta I_\ell(p_\ell) - \epsilon|$ is below a tolerance δ (we use $\delta = 0.02$), stop and set $p_\ell^* \leftarrow p_\ell$.
 - (d) If $\delta I_\ell(p_\ell) > \epsilon$ (too much information loss), decrease dropout: $p_\ell \leftarrow 0.9 p_\ell$.
 - (e) If $\delta I_\ell(p_\ell) < \epsilon$ (too little information loss), increase dropout: $p_\ell \leftarrow \min(1.1 p_\ell, 0.9)$.

This yields, for each input, an optimised rate vector $\mathbf{p}^* = (p_1^*, \dots, p_L^*)$ and per-layer iteration counts n_ℓ .

OOD scoring from variance and optimisation dynamics. Given the optimised rates \mathbf{p}^* , we run MC dropout with all layers active and fixed rates p_ℓ^* , producing $M = 30$ stochastic predictions $\{\hat{y}_m\}_{m=1}^M$ for the regression output (binding affinity in our case).

Rate-In then constructs a *scalar* OOD score by combining three signals:

1. **Predictive variance**

$$\sigma_{\text{pred}}^2 = \text{Var}(\{\hat{y}_m\}_{m=1}^M),$$

the usual MC-dropout epistemic uncertainty.

2. **Rate variance**

$$\sigma_{\text{rate}}^2 = \text{Var}(\{p_\ell^*\}_{\ell=1}^L),$$

which measures how heterogeneous the optimised dropout rates are across layers.

3. **Convergence difficulty**

$$\bar{n} = \frac{1}{L} \sum_{\ell=1}^L n_\ell,$$

the average number of iterations required to satisfy the information-loss constraint.

We combine these into a single OOD score

$$s_{\text{OOD}}(x) = \sigma_{\text{pred}}^2 + \lambda_1 \sigma_{\text{rate}}^2 + \lambda_2 \frac{\bar{n}}{N_{\text{max}}}, \quad (5.18)$$

with fixed weights $\lambda_1 = 0.3$ and $\lambda_2 = 0.2$. Large values of s_{OOD} indicate high uncertainty and/or unstable information flow, and are interpreted as evidence for OOD.

Instantiation on GEMS. We apply Rate-In to the GEMS graph neural network [3], a protein–ligand binding affinity predictor. GEMS operates on molecular graphs with rich node, edge, and global features and contains $L = 6$ dropout layers across its node/edge MLPs and global pooling blocks.

To implement Rate-In:

- We register PyTorch forward hooks on every dropout-containing module to cache $h_{\text{in}}^{(\ell)}$ and $h_{\text{out}}^{(\ell)}$ for MI estimation.
- For batched molecular graphs, activations are flattened over nodes/edges within each molecule before computing correlations.
- During rate optimisation for a given layer ℓ , we disable dropout in all other layers and iteratively adjust p_ℓ as described above.
- After obtaining \mathbf{p}^* , we enable dropout in all layers and collect M predictions to compute $s_{\text{OOD}}(x)$ via (5.18).

5.8 Author Contributions

VA developed the diffusion methodology and software stack, implementing the full pipeline from scratch for molecular complex dynamics: (i) training infrastructure (losses, conditioning, and sampling for evaluation), (ii) diffusion/noise schedules and time discretization, (iii) numerical solvers and sampling procedures, (iv) probability-flow ODE (PF-ODE) integration, and (v) likelihood evaluation via PF-ODE divergence estimation (including Hutchinson trace estimation). VA ported and integrated a modified EGNN backbone adapted from DiffSBDD into this pipeline. VA further conceived and implemented the CDCD-style unified continuous diffusion scheme to embed discrete chemical identities and continuous coordinates in a shared continuous state, enabling a single joint diffusion process and self-consistent likelihood/OOD evaluation. VA additionally designed and implemented the PF-ODE trajectory-statistics scoring features, trained the trajectory-scoring models using trajectory statistics computed by DG, implemented and trained both baselines on GEMS outputs generated by DG, and wrote the majority of the methods and the mathematical sections.

DG curated the datasets, defined the data splitting strategies, and formulated the underlying graph modeling approach. DG conducted the training of the diffusion models, implementing a custom evaluation pipeline to monitor diffusion model learning and biochemical quality metrics of sampled structures simultaneously throughout the training process. DG executed the large-scale computation of log-likelihoods and trajectory features across all datasets using a pipeline developed by VA. DG further performed the bioinformatic validation of the diffusion-based OOD scores and trained and evaluated GEMS for binding affinity predictions. Finally, DG performed the data analysis, designed the figures, and wrote the majority of the main text.

SM conceived the project and DG initiated the collaboration

RB provided advice throughout the project and critically reviewed the manuscript.

The project was supervised by SM

5.9 Acknowledgments

We thank Dr. Peter Stockinger for carefully reading the manuscript and providing valuable feedback.

S1 Supplementary Information

S1.1 Trajectory-aware OOD detection successful for 3dd0 dataset

For the dataset of alpha-carbonic anhydrases 3dd0, the PF-ODE yielded unexpectedly high log-likelihoods, which would lead to a misclassification as in-distribution (Figure S4). While log-likelihoods alone failed to identify 3dd0 complexes as OOD, we extracted additional PF-ODE trajectory statistics that capture the diffusion model’s struggle to process OOD data. In this augmented feature space, our OOD detection model can draw a clear separation between training and 3dd0 samples and successfully corrected the prediction, recognizing 3dd0 as OOD with high confidence (Table S1).

OOD detection	AUROC	Acc	F1	Spec	Prec	Recall
Traj-LDR (diffusion)	0.951 ± 0.009	0.956 ± 0.009	0.955 ± 0.009	0.976 ± 0.019	0.976 ± 0.019	0.936 ± 0.000
GEMS Rate-In	0.337 ± 0.029	0.498 ± 0.005	0.238 ± 0.317	0.641 ± 0.478	0.179 ± 0.239	0.354 ± 0.472
GEMS Embedding	0.728 ± 0.019	0.740 ± 0.012	0.764 ± 0.008	0.636 ± 0.024	0.699 ± 0.014	0.844 ± 0.000

Table S1: Trajectory-aware OOD detector identifies 3dd0 as OOD: Comparison of AUROC, accuracy (Acc), F1-Score, specificity (Spec), precision (Prec) and recall with mean \pm standard deviation across OOD datasets for the trajectory-aware LDR diffusion-based detector (Traj-LDR), the embedding-space GEMS baseline, and the Rate-In baseline. The trajectory-aware OOD detector classifies the dataset of alpha-carbonic anhydrases (3dd0) as out-of-distribution with high confidence. In contrast, the GEMS-based baselines show reduced separation capability.

S1.2 Error-log-likelihood relation

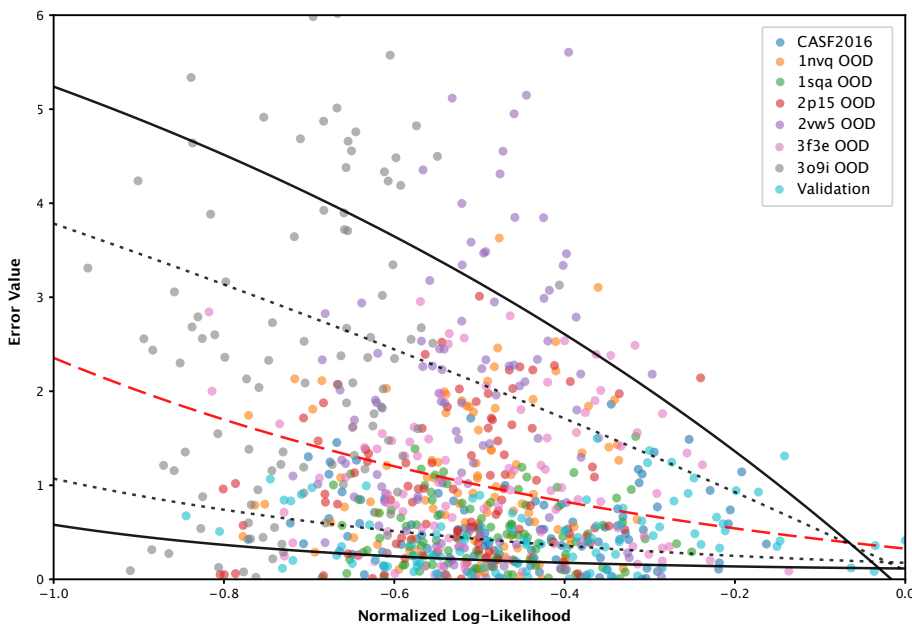


Figure S1: Error-log-likelihood relation follows a scaled a shifted exponential: Scatterplot illustrating the relationship between the log-likelihoods assigned by the diffusion model (x-axis) and the corresponding GEMS binding affinity prediction errors (y-axis) across the validation, CASF2016, and the out-of-distribution (OOD) datasets. A hierarchical fitting of five scaled and shifted exponential curves shows that log-likelihoods provide a rough estimate of the expected GEMS prediction error. Across all non-training complexes ($N = 6223$), 75.8% had predicted errors that fell within the bounds of the fitted exponential curves, with 8.84% high outliers (errors above the fit) and 15.39% low outliers (errors below the fit). To allow fair comparison across datasets with different label spreads, absolute errors are normalized by the label variance, preventing artificially low error values on narrowly distributed datasets. Exponential curves are fit to a maximum of 500 randomly sampled points from each non-training distribution. Only 100 randomly sampled complexes from each datasets are shown in the to improve visibility.

S1.3 Trajectory feature importance

To understand which aspects of the PF-ODE trajectory drive separation between in-distribution (ID) and out-of-distribution (OOD) complexes, we quantify the importance of each of our $d = 19$ trajectory statistics and rank them accordingly. Rather than reporting a single heuristic, we use a *combined importance score* that rewards features which (i) separate ID and OOD strongly and (ii) do so consistently across complexes and bootstrap splits. Concretely, for each feature we compute an effect size between ID and OOD summaries (e.g. Cohen’s d) and a stability term (e.g. variance ratio / robustness under resampling), standardize these quantities across features, and aggregate them (additively) into one score.

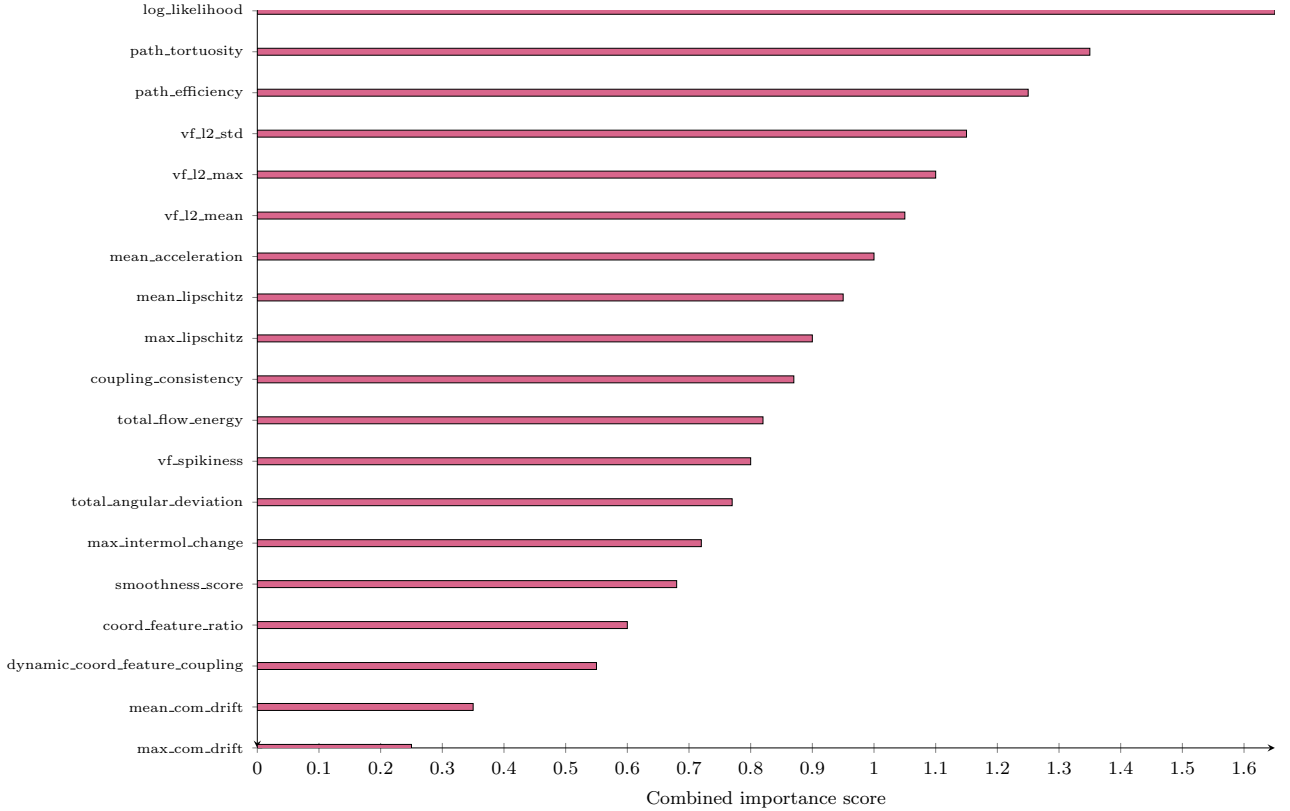


Figure S2: Top PF-ODE trajectory features ranked by a combined importance score (separation strength + stability under resampling).

Several patterns stand out. First, PF-ODE log-likelihood is the single most discriminative coordinate, but it is not the whole story: multiple trajectory descriptors achieve comparable importance, confirming that OOD shift manifests as a *dynamic* signature along the probability flow rather than only as a terminal density value. Second, the highest-ranked non-likelihood features cluster into interpretable families: (i) *path geometry* (tortuosity/efficiency), indicating that OOD inputs induce longer and less direct transport to noise; (ii) *field magnitude and burstiness* (vf.l2 mean/max/std and spikiness), indicating larger and more intermittent corrective updates; and (iii) *stability and smoothness* (Lipschitz and acceleration), indicating stiffer and less temporally regular dynamics. Finally, coupling-related terms (e.g. coupling_consistency and dynamic_coord_feature_coupling) rank non-trivially, suggesting that OOD behavior is not purely geometric: atypical complexes also perturb how coordinate and identity updates co-evolve across noise scales.

S1.4 Evaluation of sensitivity to ligand size and chemical features

Naturally, the size of the input ligand and pocket influence the PF-ODE log-likelihood scores. As anticipated, datasets with significant divergence in ligand and pocket size distributions relative to the training data generally received lower scores, indicating OOD status. However, the diffusion model demonstrated a notable robustness to this size-induced distribution shift. Many complexes containing extraordinarily large ligands were nonetheless assigned high log-likelihoods, indicating that size is not the sole driver of the OOD signal. This resilience is exemplified by the 3f3e dataset: Despite possessing by far the largest ligand and pocket sizes (Figure S3), it yielded intermediate log-likelihoods. This suggests an intermediate OOD status, a conclusion which was confirmed by our bioinformatic OOD quantification (Figure 2), which identified 3f3e to present a moderate distribution shift relative to the training data. This suggests that the diffusion model recognizes familiar structural motifs and assigns high likelihoods, even when the input’s size strongly deviates from the common sizes in the training distribution.

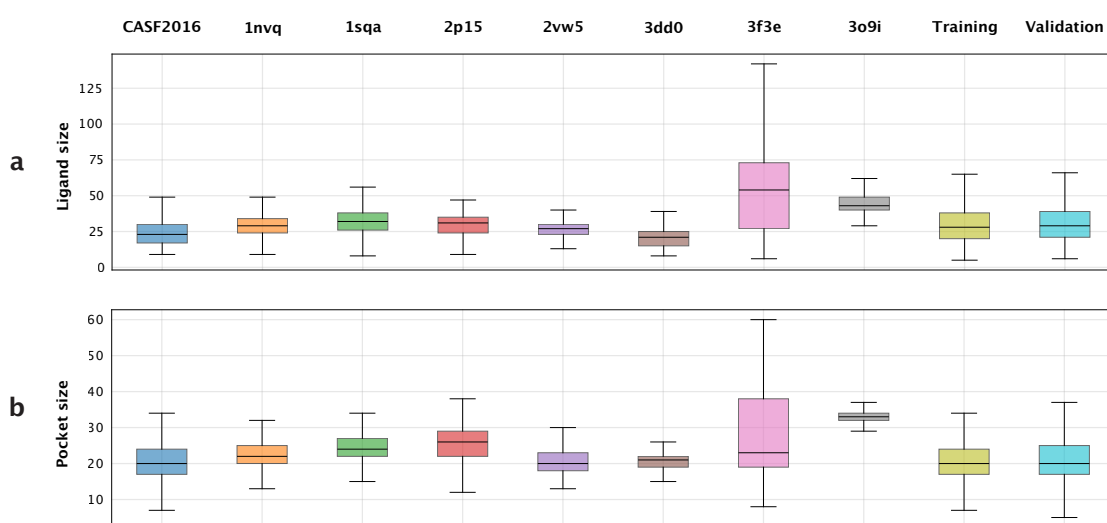


Figure S3: Ligand and Pocket Size Distribution Across Datasets: This figure compares the distributions of **a)** ligand sizes (atom counts) and **b)** protein pocket sizes (amino acid counts) across all datasets, including CASF2016 ($N = 281$), 1nvq ($N = 2684$), 1sqa ($N = 734$), 2p15 ($N = 455$), 2vw5 ($N = 207$), 3dd0 ($N = 461$), 3f3e ($N = 389$), 3o9i ($N = 468$), training ($N = 10'168$) and validation ($N = 1'127$) datasets. As pocket residues are determined using a fixed radius around each ligand atom, ligand and pocket sizes are strongly connected. Boxplots show the median (centre line), 25th–75th percentiles (box), whiskers extend to data points within $1.5 \times \text{IQR}$, outliers are not shown.

A notable limitation of our diffusion model is the limited sensitivity to unique chemistry. We observed that the model struggles to detect distribution shifts when unique chemistry is masked by common geometries. In this context, the carbonic anhydrase dataset 3dd0 presented a distinct challenge. This cluster of metalloenzymes was consistently assigned high log-likelihoods (Figure S4) despite containing chemical features that are underrepresented in the training distribution, such as zinc ions and sulfonamide-rich ligands. Visual inspection reveals that these ligands often possess simple, generic scaffolds. This implies that the current diffusion model may overemphasize geometric familiarity at the expense of recognizing specific, rare chemical substructures.

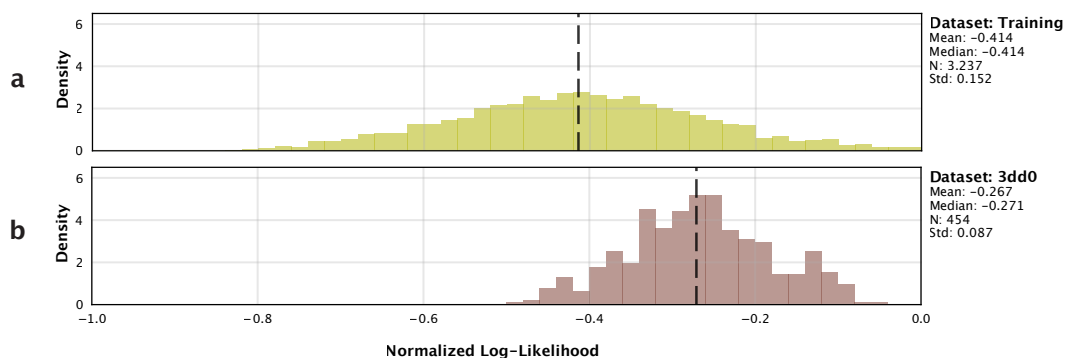


Figure S4: OOD dataset 3dd0 yields high log-likelihoods: Distributions of log-likelihoods assigned to protein-ligand complexes belonging to the a) training and b) 3dd0 dataset of alpha carbonic anhydrases. Lower values signify increased deviation from the learned distribution (OOD) and higher values indicate high in-distribution (ID) probability. Means, medians, standard deviations (Std) and number of samples (N) are depicted on the right side of the histograms. Vertical dashed lines indicate the median of the respective log-likelihood distributions. The training distribution was randomly subsampled, showing only a fraction of all 10^5 complexes.

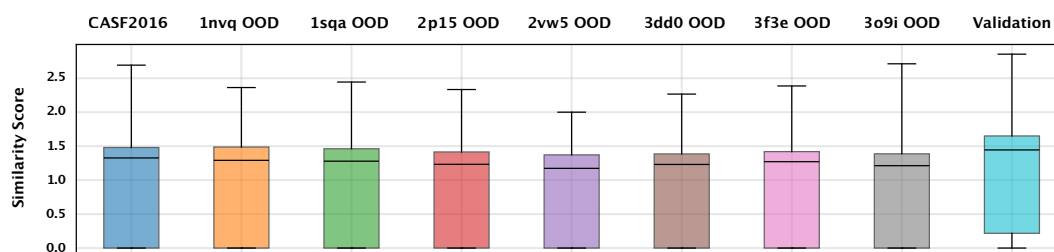


Figure S5: Distributions of train-test aggregated similarity scores: A composite score $S = \max(\text{Tanimoto} + \text{TM Score} + (1 - \text{RMSD}), 0)$ was calculated as the sum of Tanimoto similarity, TM-scores, and inverted pocket-aligned ligand root mean squared deviation (RMSD). High scores signify highly similar protein-ligand complexes (3.0 = identical complexes). Each box represents the distribution of $N = 10,510$ similarity scores. Specifically, these are the scores between each training dataset complex and its most similar counterpart in the respective test dataset, as measured by that specific metric. Boxplots show the median (centre line), 25th–75th percentiles (box), whiskers extend to data points within $1.5 \times \text{IQR}$, outliers are not shown.

S1.5 Intra-Cluster Ligand Diversity

While we isolated specific protein families into OOD datasets, the ligand space remained uncontrolled. Consequently, OOD pockets bind a diverse mix of ligands, ranging from familiar to exotic structures. Figure S6 shows the intra-cluster ligand diversity of each dataset. For every dataset, we identified a medoid ligand, defined as the molecule with the smallest sum of distances ($1 - \text{Tanimoto similarity}$) to all other ligands, and computed the distance of all other ligands to this central reference.

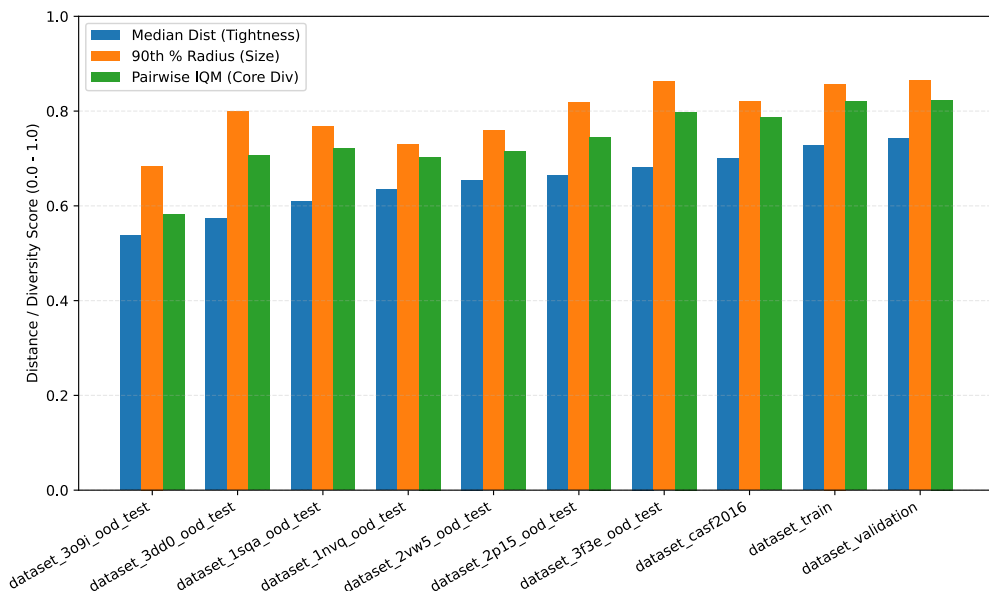


Figure S6: Intra-cluster ligand diversity of all datasets sorted by cluster tightness in ascending order. Three robust intra-cluster diversity metrics are included: (1 median distance to medoid measures typical cluster tightness by computing the median distance from the most representative point to all other points; (2 90th percentile radius captures robust cluster size by identifying the distance that encompasses 90% of points from the medoid; and (3 pairwise inter-quartile mean (IQM) quantifies overall cluster cohesion by averaging distances between all unique pairs within the middle 50% of the pairwise distance distribution, providing resistance to outliers.

S1.6 Sampling Evaluation

The distribution-learning performance of the diffusion model was tested by quality checks on sampled graphs during model training. The validity of the *de novo* generated protein–ligand configurations was assessed using the following metrics:

- Divergence of atom type distribution from training distribution
- Divergence of amino acid type distribution from training distribution
- Percentage of fragmented ligands and mean number of fragments after bond inference
- Chemical validity (RDKit sanitization success)
- Mean number of rings and mean ring size per molecule

The best model achieved 92% chemical validity, 84% unfragmented ligands, and an average of 2.72 rings per ligand with a mean ring size of 5.59. Divergences in atom and amino acid type distributions (Jensen–Shannon) from the training data were low, at 0.010 and 0.009, respectively. These results indicate that the model learned the training distribution well enough to effectively map Gaussian noise to realistic 3D atom placements, resulting in chemically valid *de novo* ligands.

S1.7 PF-ODE likelihoods as predictors of predictive error

We formalize the connection between the probability–flow ODE (PF-ODE) log-likelihoods assigned by the diffusion model and the prediction errors of an independent binding-affinity model such as GEMS. Throughout, x denotes a protein–ligand complex represented as a graph with 3D coordinates and discrete atom/residue types (Section 5.2).

Two-model setting. Let p_0 be the (unknown) data distribution on complexes, assumed to admit a density $p_0(x)$ with respect to Lebesgue measure on the ambient Euclidean space (COM-centered coordinates concatenated with continuous embeddings). We train:

- a *diffusion model* with PF-ODE density $q_\phi(x)$ and score field $s_\phi(x, t)$, parameterised by ϕ , and

- an *independent predictor* (e.g. GEMS) with parameters θ , which for each input x outputs a scalar prediction $\hat{y}_\theta(x)$ of the true binding affinity $y(x)$.

We define the pointwise prediction error as

$$e_\theta(x) := |\hat{y}_\theta(x) - y(x)|, \quad (\text{S1.1})$$

or its variance-normalised version used in our experiments (Section 2.4).

The diffusion model yields a per-complex log-likelihood via the PF-ODE (Section 5.2.3); we write

$$\ell_\phi(x) := \log q_\phi(x), \quad L_\phi(x) := -\ell_\phi(x) = -\log q_\phi(x), \quad (\text{S1.2})$$

for the log-likelihood and the negative log-likelihood (NLL), respectively. In what follows we omit the subscript ϕ when unambiguous and write q, q_t, s instead of q_ϕ, q_t^ϕ, s_ϕ .

Our goal in this section is to relate $L(x)$, which is fully determined by the diffusion model, to the error $e_\theta(x)$ of the *separate* predictive model, under explicit and mild assumptions.

S1.7.1 Relative entropy along the PF-ODE

We recall the PF-ODE setup from Section 5.2. Let $\{p_t\}_{t \in [0,1]}$ and $\{q_t\}_{t \in [0,1]}$ be the time-marginal densities of the noising process and the learned PF-ODE, respectively, so that

$$p_t(x) = p(x_t = x), \quad q_t(x) = q_\phi(x_t = x). \quad (\text{S1.3})$$

The true and learned PF-ODE drifts are denoted by $v^*(x, t)$ and $v_\phi(x, t)$, and both families satisfy the continuity equations

$$\partial_t p_t(x) = -\nabla_x \cdot (p_t(x) v^*(x, t)), \quad \partial_t q_t(x) = -\nabla_x \cdot (q_t(x) v_\phi(x, t)). \quad (\text{S1.4})$$

Assumption S1.1 (Regularity of the PF-ODE marginals). For every $t \in [0, 1]$ the densities p_t and q_t are smooth and strictly positive on \mathbb{R}^d , and satisfy sufficient decay at infinity so that:

- differentiation under the integral sign is justified;
- integration by parts over \mathbb{R}^d produces no boundary terms.

Interpretation. This is a standard smoothness and decay assumption for continuity equations and PF-ODEs. In our setting, p_1 and q_1 are equal to the same COM-constrained Gaussian (Section 5.2.3), and the PF-ODE preserves smoothness when started from smooth data.

KL divergence and relative Fisher information. For each $t \in [0, 1]$ we define the relative entropy (KL divergence) and relative Fisher information between p_t and q_t as

$$D_t := \text{KL}(p_t \parallel q_t) = \int_{\mathbb{R}^d} p_t(x) \log \frac{p_t(x)}{q_t(x)} dx, \quad (\text{S1.5})$$

$$I_t := \int_{\mathbb{R}^d} p_t(x) \|\nabla_x \log p_t(x) - \nabla_x \log q_t(x)\|_2^2 dx. \quad (\text{S1.6})$$

In our molecular setting, x contains all COM-centered coordinates and continuous embeddings of atoms and residues, stacked into a single Euclidean vector.

Lemma S1.2 (Time derivative of KL along the PF-ODE). *Under Assumption S1.1,*

$$\frac{d}{dt} D_t = \int_{\mathbb{R}^d} p_t(x) (v^*(x, t) - v_\phi(x, t))^\top \left[\nabla_x \log p_t(x) - \nabla_x \log q_t(x) \right] dx. \quad (\text{S1.7})$$

Proof. Starting from the definition (S1.5),

$$\frac{d}{dt}D_t = \frac{d}{dt} \int_{\mathbb{R}^d} p_t(x) \log \frac{p_t(x)}{q_t(x)} dx \quad (\text{S1.8})$$

$$= \int_{\mathbb{R}^d} (\partial_t p_t(x)) \log \frac{p_t(x)}{q_t(x)} dx + \int_{\mathbb{R}^d} p_t(x) \partial_t \log \frac{p_t(x)}{q_t(x)} dx. \quad (\text{S1.9})$$

For the second term we expand

$$\partial_t \log \frac{p_t}{q_t} = \frac{\partial_t p_t}{p_t} - \frac{\partial_t q_t}{q_t}, \quad (\text{S1.10})$$

so that

$$\int p_t \partial_t \log \frac{p_t}{q_t} dx = \int \partial_t p_t(x) dx - \int \frac{p_t(x)}{q_t(x)} \partial_t q_t(x) dx. \quad (\text{S1.11})$$

Because p_t is a probability density, $\int \partial_t p_t dx = \partial_t \int p_t dx = 0$, hence

$$\frac{d}{dt}D_t = \int (\partial_t p_t) \log \frac{p_t}{q_t} dx - \int \frac{p_t}{q_t} \partial_t q_t dx. \quad (\text{S1.12})$$

Using the continuity equations

$$\partial_t p_t = -\nabla_x \cdot (p_t v^*), \quad \partial_t q_t = -\nabla_x \cdot (q_t v_\phi), \quad (\text{S1.13})$$

we obtain

$$\frac{d}{dt}D_t = - \int \nabla_x \cdot (p_t v^*) \log \frac{p_t}{q_t} dx + \int \frac{p_t}{q_t} \nabla_x \cdot (q_t v_\phi) dx. \quad (\text{S1.14})$$

Assumption S1.1 allows us to integrate by parts without boundary terms. For the first term,

$$- \int \nabla_x \cdot (p_t v^*) \log \frac{p_t}{q_t} dx = \int p_t(x) v^*(x, t) \cdot \nabla_x \log \frac{p_t(x)}{q_t(x)} dx. \quad (\text{S1.15})$$

For the second term,

$$\int \frac{p_t}{q_t} \nabla_x \cdot (q_t v_\phi) dx = - \int q_t(x) v_\phi(x, t) \cdot \nabla_x \left(\frac{p_t(x)}{q_t(x)} \right) dx \quad (\text{S1.16})$$

$$= - \int p_t(x) v_\phi(x, t) \cdot \nabla_x \log \frac{p_t(x)}{q_t(x)} dx. \quad (\text{S1.17})$$

Combining these identities gives

$$\frac{d}{dt}D_t = \int p_t(x) (v^*(x, t) - v_\phi(x, t)) \cdot \nabla_x \log \frac{p_t(x)}{q_t(x)} dx, \quad (\text{S1.18})$$

which is (S1.7). \square

Interpretation. Lemma S1.2 is an exact information-balance identity: the rate of change of the KL divergence between the true and learned PF-ODE marginals is the inner product, averaged under p_t , between (i) the velocity mismatch $v^* - v_\phi$ and (ii) the gradient of the log-density ratio $\log \frac{p_t}{q_t}$.

Lemma S1.3 (Cauchy–Schwarz bound on \dot{D}_t). *Under the assumptions above,*

$$|\dot{D}_t| \leq \left(\int_{\mathbb{R}^d} p_t(x) \|v^*(x, t) - v_\phi(x, t)\|_2^2 dx \right)^{1/2} \sqrt{I_t}, \quad (\text{S1.19})$$

where I_t is the relative Fisher information from (S1.6).

Proof. Apply the Cauchy–Schwarz inequality to (S1.7). \square

Interpretation. The instantaneous rate of change of KL is bounded by the product of two factors: (i) the root-mean-squared velocity error between the true and learned PF-ODEs, and (ii) the square root of the Fisher information of the log-density ratio.

Relation to score error. In our VE setting, the PF-ODE drifts and scores are linked by

$$v^*(x, t) = -\frac{1}{2}g(t)^2 s^*(x, t), \quad v_\phi(x, t) = -\frac{1}{2}g(t)^2 s_\phi(x, t), \quad (\text{S1.20})$$

with scalar diffusion coefficient $g(t)$. Hence

$$v^*(x, t) - v_\phi(x, t) = -\frac{1}{2}g(t)^2 (s^*(x, t) - s_\phi(x, t)). \quad (\text{S1.21})$$

Define

$$A_t := \int_{\mathbb{R}^d} p_t(x) \|v^*(x, t) - v_\phi(x, t)\|_2^2 dx. \quad (\text{S1.22})$$

Then

$$A_t = \frac{g(t)^4}{4} \int_{\mathbb{R}^d} p_t(x) \|s^*(x, t) - s_\phi(x, t)\|_2^2 dx. \quad (\text{S1.23})$$

We quantify the time-integrated score error as

$$\mathcal{L}_{\text{score}}(\phi) := \int_0^1 g(t)^4 \int_{\mathbb{R}^d} p_t(x) \|s^*(x, t) - s_\phi(x, t)\|_2^2 dx dt, \quad (\text{S1.24})$$

which differs from the practical training loss only by a known time-dependent weight (Section 5.2).

With this definition,

$$\int_0^1 A_t dt = \frac{1}{4} \mathcal{L}_{\text{score}}(\phi). \quad (\text{S1.25})$$

Integrating (S1.19) in time from $t = 0$ to $t = 1$ and using that $D_1 = \text{KL}(p_1 \| q_1) = 0$ (common terminal Gaussian under COM constraints), we obtain we obtain

$$D_0 = -\int_0^1 \dot{D}_t dt \leq \int_0^1 |\dot{D}_t| dt \leq \int_0^1 \sqrt{A_t I_t} dt. \quad (\text{S1.26})$$

Another application of Cauchy–Schwarz in time yields

$$D_0 \leq \left(\int_0^1 A_t dt \right)^{1/2} \left(\int_0^1 I_t dt \right)^{1/2} = \frac{1}{2} \sqrt{\mathcal{L}_{\text{score}}(\phi)} \left(\int_0^1 I_t dt \right)^{1/2}. \quad (\text{S1.27})$$

Assumption S1.4 (Bounded integrated relative Fisher). There exists a constant $C_{\text{FI}} > 0$ such that

$$\int_0^1 I_t dt \leq C_{\text{FI}}. \quad (\text{S1.28})$$

Interpretation. Assumption S1.4 states that the time-integrated relative Fisher information between the true and learned marginals remains bounded. In other words, along the entire PF-ODE trajectory the score fields $\nabla_x \log p_t$ and $\nabla_x \log q_t$ do not develop arbitrarily large discrepancies in gradient norm. When $q_t = p_t$ for all t (perfect modelling), we have $I_t \equiv 0$, so the assumption trivially holds.

Combining (S1.27) with Assumption S1.4 yields:

Proposition S1.5 (Score error controls final-time KL up to capacity). *Under Assumptions S1.1 and S1.4,*

$$\text{KL}(p_0 \| q_0) = D_0 \leq \frac{1}{2} \sqrt{C_{\text{FI}}} \sqrt{\mathcal{L}_{\text{score}}(\phi)}. \quad (\text{S1.29})$$

Interpretation. Proposition S1.5 states that if the PF-ODE velocity field learned by the diffusion model tracks the true probability-flow velocity field in mean-squared sense (small $\mathcal{L}_{\text{score}}$), and if the relative Fisher information along the flow stays bounded, then the resulting density q_0 is close to the true data distribution p_0 in KL. In our context, this means that a well-trained molecular diffusion model assigns a globally reasonable density to the ensemble of protein-ligand complexes seen during training.

S1.7.2 PF-ODE negative log-likelihood as a random variable

We now treat the PF-ODE negative log-likelihood

$$L(x) := -\log q_0(x) \quad (\text{S1.30})$$

as a random variable under the data distribution p_0 .

The Shannon entropy of p_0 is

$$H(p_0) := -\int_{\mathbb{R}^d} p_0(x) \log p_0(x) dx. \quad (\text{S1.31})$$

By the definition of KL divergence,

$$\text{KL}(p_0||q_0) = \int_{\mathbb{R}^d} p_0(x) \log \frac{p_0(x)}{q_0(x)} dx \quad (\text{S1.32})$$

$$= \int_{\mathbb{R}^d} p_0(x) \log p_0(x) dx - \int_{\mathbb{R}^d} p_0(x) \log q_0(x) dx \quad (\text{S1.33})$$

$$= -H(p_0) + \int_{\mathbb{R}^d} p_0(x) L(x) dx. \quad (\text{S1.34})$$

Rearranging gives the exact identity

$$\int_{\mathbb{R}^d} p_0(x) L(x) dx = H(p_0) + \text{KL}(p_0||q_0). \quad (\text{S1.35})$$

We denote this typical (mean) NLL by

$$L_{\text{typ}} := \int_{\mathbb{R}^d} p_0(x) L(x) dx = H(p_0) + \text{KL}(p_0||q_0). \quad (\text{S1.36})$$

Interpretation. The mean PF-ODE NLL under the true data distribution decomposes into an intrinsic term (the entropy $H(p_0)$) and a mismatch term ($\text{KL}(p_0||q_0)$). Proposition S1.5 implies that $\text{KL}(p_0||q_0)$ is small when the diffusion model is well-trained, so L_{typ} is close to the intrinsic complexity of p_0 .

Assumption S1.6 (Finite NLL variance). There exists a constant $\sigma^2 < \infty$ such that

$$\text{Var}_{x \sim p_0}(L(x)) = \int_{\mathbb{R}^d} p_0(x) (L(x) - L_{\text{typ}})^2 dx \leq \sigma^2. \quad (\text{S1.37})$$

Interpretation. Assumption S1.6 requires that the PF-ODE NLL does not exhibit infinite variance under the training distribution. For any sane trained density model this holds in practice and imposes a minimal regularity condition on the tails of q_0 with respect to p_0 .

Under this assumption, a basic Chebyshev bound yields tail control:

Lemma S1.7 (NLL concentration under p_0). *Under Assumption S1.6, for any $\alpha > 0$,*

$$\int_{\{x: L(x) \geq L_{\text{typ}} + \alpha\}} p_0(x) dx \leq \frac{\sigma^2}{\alpha^2}. \quad (\text{S1.38})$$

Proof. Apply Chebyshev's inequality to the centered random variable $Z(x) := L(x) - L_{\text{typ}}$:

$$\int_{\{x: |Z(x)| \geq \alpha\}} p_0(x) dx \leq \frac{\text{Var}_{p_0}(Z)}{\alpha^2} \leq \frac{\sigma^2}{\alpha^2}. \quad (\text{S1.39})$$

Since the event $\{L(x) \geq L_{\text{typ}} + \alpha\}$ is contained in $\{|Z(x)| \geq \alpha\}$, the same bound holds for (S1.38). \square

Lemma S1.7 provides a minimal concentration statement: most training complexes have PF-ODE NLLs within a band of width $O(\alpha)$ around the typical value L_{typ} , with a tail probability decaying at least as $1/\alpha^2$.

S1.7.3 Coupling PF-ODE likelihoods to GEMS errors

We now link the PF-ODE NLL $L(x)$ of the diffusion model to the prediction error $e_\theta(x)$ of an independent model such as GEMS. In our experiments (Section 2.4), we observe a strong empirical relationship between PF-ODE log-likelihoods and GEMS binding-affinity errors: complexes with low likelihood (high $L(x)$) tend to exhibit large prediction errors, whereas high-likelihood complexes have much smaller errors on average.

We capture this relationship by a monotone error envelope:

Assumption S1.8 (Monotone NLL-error envelope). There exists a non-decreasing function $\phi : \mathbb{R} \rightarrow [0, \infty)$ such that, for p_0 -almost every complex x ,

$$e_\theta(x) \leq \phi(L(x)). \quad (\text{S1.40})$$

Assumption S1.8 states that for any two complexes x_1, x_2 with $L(x_1) \leq L(x_2)$ (i.e. x_1 is at least as likely as x_2 under the diffusion model), the worst-case prediction error at x_1 is no larger than the worst-case error at x_2 . The function ϕ acts as a *calibration curve* mapping PF-ODE NLL values to an upper bound on the predictive error. In practice, ϕ can be obtained empirically by fitting a non-decreasing upper envelope (e.g. a scaled and shifted exponential) to the scatter plot of $(L(x), e_\theta(x))$ on a held-out calibration set (Figure S1). This is in accordance with the further empirical findings explained in Section 2.4; for visualizations, refer to Figures 3 and 4 in the main text.

Theorem S1.9 (High-probability error bound from PF-ODE NLL). *Suppose Assumptions S1.1, S1.4, S1.6, and S1.8 hold, and that the VE relation between velocities and scores in Section 5.2 is satisfied. Let L_{typ} denote the typical NLL under p_0 , and fix any margin $\alpha > 0$. Then*

$$\int_{\{x: e_\theta(x) > \phi(L_{\text{typ}} + \alpha)\}} p_0(x) dx \leq \frac{\sigma^2}{\alpha^2}. \quad (\text{S1.41})$$

Equivalently,

$$\mathbb{P}_{x \sim p_0} \left(e_\theta(x) \leq \phi(L_{\text{typ}} + \alpha) \right) \geq 1 - \frac{\sigma^2}{\alpha^2}. \quad (\text{S1.42})$$

Proof. Consider the event

$$A_\alpha := \{x : L(x) \leq L_{\text{typ}} + \alpha\}. \quad (\text{S1.43})$$

On A_α , Assumption S1.8 and monotonicity of ϕ yield

$$e_\theta(x) \leq \phi(L(x)) \leq \phi(L_{\text{typ}} + \alpha) \quad \text{for all } x \in A_\alpha. \quad (\text{S1.44})$$

Therefore the event $\{x : e_\theta(x) > \phi(L_{\text{typ}} + \alpha)\}$ is contained in the complement A_α^c , and

$$\int_{\{x: e_\theta(x) > \phi(L_{\text{typ}} + \alpha)\}} p_0(x) dx \leq \int_{A_\alpha^c} p_0(x) dx = \int_{\{x: L(x) > L_{\text{typ}} + \alpha\}} p_0(x) dx. \quad (\text{S1.45})$$

Applying Lemma S1.7 to the right-hand side,

$$\int_{\{x: L(x) > L_{\text{typ}} + \alpha\}} p_0(x) dx \leq \frac{\sigma^2}{\alpha^2}, \quad (\text{S1.46})$$

which establishes (S1.41). \square

Theorem S1.9 makes the following statement in our concrete setting:

- The diffusion model is trained on the same structural distribution of protein-ligand complexes as GEMS, but using only 3D geometry and discrete types (no affinities).
- If the PF-ODE is well trained (small score loss $\mathcal{L}_{\text{score}}(\phi)$) and its density q_0 does not have pathological NLL variance, then there exists a typical NLL level L_{typ} such that:

On almost all in-distribution complexes (all but a fraction $O(\sigma^2/\alpha^2)$), a near-typical PF-ODE NLL $L(x) \leq L_{\text{typ}} + \alpha$ implies a uniform upper bound on the GEMS prediction error: $e_\theta(x) \leq \phi(L_{\text{typ}} + \alpha)$.

- Conversely, complexes with unusually high PF-ODE NLL $L(x) \gg L_{\text{typ}}$ fall outside this guarantee. For such complexes the theorem does not enforce any small error bound, which is consistent with our empirical observation that low-likelihood complexes exhibit heavy-tailed GEMS errors (Figures 4 and S1).

From a practical perspective, PF-ODE log-likelihoods provide a task-agnostic, generative notion of “typicality” for protein-ligand complexes. Theorem S1.9 explains why these likelihoods can serve as a useful proxy for the reliability of a separate predictive model such as GEMS: up to smoothness and concentration assumptions, being high-likelihood under the diffusion model is a sufficient condition for having small prediction error with high probability under the training distribution.

S1.8 Comprehensive Error Tables

Dataset	AUROC	Acc	F1	Spec	Prec	Recall
casf2016	0.554 ± 0.019	0.558 ± 0.016	0.559 ± 0.009	0.557 ± 0.032	0.559 ± 0.018	0.559 ± 0.000
1nvq	0.804 ± 0.007	0.785 ± 0.005	0.803 ± 0.004	0.694 ± 0.009	0.741 ± 0.006	0.876 ± 0.000
1sqa	0.928 ± 0.008	0.830 ± 0.007	0.818 ± 0.006	0.899 ± 0.013	0.883 ± 0.013	0.762 ± 0.000
2p15	0.721 ± 0.017	0.585 ± 0.010	0.473 ± 0.006	0.797 ± 0.020	0.649 ± 0.022	0.373 ± 0.000
2vw5	0.659 ± 0.033	0.715 ± 0.020	0.753 ± 0.013	0.564 ± 0.039	0.666 ± 0.021	0.866 ± 0.000
3f3e	0.919 ± 0.009	0.824 ± 0.007	0.804 ± 0.007	0.926 ± 0.015	0.907 ± 0.017	0.722 ± 0.000
3o9i	0.922 ± 0.010	0.866 ± 0.008	0.862 ± 0.007	0.895 ± 0.016	0.888 ± 0.015	0.837 ± 0.000

Table S2: Embedding-space GEMS baseline OOD detection performance across held-out splits. For each dataset, we report the mean ± standard deviation of AUROC, accuracy (Acc), F1, and specificity (Spec) over balanced bootstrap test subsets, treating OOD as the positive class. For each split we take the *best* detector by AUROC among Mahalanobis, k -NN distance, Local Outlier Factor, Isolation Forest and one-class SVM. The final rows report the mean and standard deviation across datasets for these summary metrics. Per-dataset precision (Prec) and recall of the embedding-space GEMS baseline, using the best detector per dataset selected by AUROC. We report mean ± standard deviation over balanced bootstrap test subsets, with OOD as the positive class.

Dataset	AUROC	Acc	F1	Spec	Prec	Recall
casf2016	0.708 ± 0.042	0.604 ± 0.029	0.449 ± 0.018	0.887 ± 0.058	0.753 ± 0.100	0.321 ± 0.000
1nvq	0.842 ± 0.013	0.744 ± 0.011	0.736 ± 0.009	0.776 ± 0.023	0.761 ± 0.018	0.712 ± 0.000
1sqa	0.888 ± 0.013	0.787 ± 0.014	0.758 ± 0.012	0.906 ± 0.027	0.878 ± 0.031	0.667 ± 0.000
2p15	0.754 ± 0.034	0.693 ± 0.027	0.680 ± 0.019	0.734 ± 0.054	0.713 ± 0.043	0.651 ± 0.000
2vw5	0.939 ± 0.033	0.888 ± 0.028	0.886 ± 0.025	0.912 ± 0.057	0.911 ± 0.053	0.864 ± 0.000
3f3e	0.639 ± 0.061	0.598 ± 0.035	0.429 ± 0.021	0.897 ± 0.070	0.765 ± 0.125	0.300 ± 0.000
3o9i	0.963 ± 0.006	0.949 ± 0.011	0.948 ± 0.011	0.986 ± 0.022	0.985 ± 0.023	0.913 ± 0.000

Table S3: Performance of the trajectory-aware LDR OOD detector across held-out splits: For each OOD dataset, we report the mean ± standard deviation of AUROC, accuracy (Acc), F1, specificity (Spec), Precision (Prec) and recall over balanced bootstrap test subsets, treating OOD as the positive class.

The embedding-based baseline achieved a respectable mean AUROC of 0.78 and F1-score of 0.73 across all datasets. However, performance was highly inconsistent. While it effectively detected anomalies in some distinct OOD splits (e.g., HIV proteases), it degraded to near-random guessing on challenging datasets with moderate distribution shift like CASF2016. This baseline serves as a strong and interpretable reference for our experiments, demonstrating what is achievable using post-hoc analysis of fixed representations. Overall, it systematically underperformed the trajectory-aware OOD classifier, which leverages multiple trajectory statistics derived from our diffusion model.

Dataset	AUROC	Acc	F1	Spec	Prec	Recall
casf2016	0.444 ± 0.041	0.492 ± 0.027	0.605 ± 0.100	0.169 ± 0.154	0.484 ± 0.072	0.815 ± 0.172
1nvq	0.581 ± 0.013	0.584 ± 0.009	0.645 ± 0.016	0.411 ± 0.045	0.562 ± 0.008	0.757 ± 0.045
1sqa	0.664 ± 0.024	0.642 ± 0.021	0.667 ± 0.021	0.565 ± 0.050	0.624 ± 0.021	0.718 ± 0.042
2p15	0.541 ± 0.039	0.545 ± 0.030	0.616 ± 0.042	0.350 ± 0.116	0.534 ± 0.024	0.740 ± 0.111
2vw5	0.439 ± 0.047	0.487 ± 0.024	0.586 ± 0.135	0.180 ± 0.221	0.470 ± 0.098	0.795 ± 0.233
3f3e	0.741 ± 0.032	0.690 ± 0.030	0.649 ± 0.034	0.806 ± 0.054	0.750 ± 0.047	0.574 ± 0.046
3o9i	0.859 ± 0.024	0.828 ± 0.022	0.838 ± 0.021	0.764 ± 0.038	0.791 ± 0.027	0.892 ± 0.029
validation	0.503 ± 0.022	0.501 ± 0.015	0.533 ± 0.131	0.365 ± 0.250	0.495 ± 0.053	0.638 ± 0.254

Table S4: Rate-In OOD Detection Performance: For each OOD dataset, we report the mean \pm standard deviation of AUROC, accuracy (Acc), F1, and specificity (Spec) over 100 bootstrap iterations with 70/30 train/test splits, treating OOD as the positive class. The final rows report the mean and standard deviation across datasets for these summary metrics. For each OOD dataset, we report precision and recall over 100 bootstrap iterations.

References

- [1] R. Wang, X. Fang, Y. Lu, and S. Wang, “The PDBbind database: Collection of binding affinities for protein-ligand complexes with known three-dimensional structures,” *Journal of Medicinal Chemistry*, vol. 47, no. 12, pp. 2977–2980, 2004. PDBbind Database.
- [2] Z. Liu, Y. Li, L. Han, J. Li, J. Liu, Z. Zhao, W. Nie, Y. Liu, and R. Wang, “PDB-wide collection of binding data: current status of the PDBbind database,” *Bioinformatics*, vol. 31, no. 3, pp. 405–412, 2015. PDBbind Database.
- [3] D. Graber, P. Stockinger, F. Meyer, S. Mishra, C. Horn, and R. Buller, “Resolving data bias improves generalization in binding affinity prediction,” *Nature Machine Intelligence*, vol. 7, no. 10, pp. 1713–1725, 2025.
- [4] RCSB Protein Data Bank, “Pdb growth statistics.” <https://www.rcsb.org/stats/growth/growth-released-structures>, 2025. Accessed 2025-12-15.
- [5] J. Li and X. Gong, “Harnessing pre-trained models for accurate prediction of protein-ligand binding affinity,” *BMC bioinformatics*, vol. 26, no. 1, pp. 1–21, 2025.
- [6] M. Su, Q. Yang, Y. Du, G. Feng, Z. Liu, Y. Li, and R. Wang, “Comparative assessment of scoring functions: The CASF-2016 update,” *Journal of Chemical Information and Modeling*, vol. 59, no. 2, pp. 895–913, 2019. CASF2016.
- [7] J. Kopko, D. Graber, S. M. Eyrilmez, S. Mazurenko, D. Bednar, J. Sedlar, and J. Sivic, “Generalization beyond benchmarks: Evaluating learnable protein-ligand scoring functions on unseen targets,” *arXiv preprint arXiv:2512.05386*, 2025.
- [8] Y. Zhang and J. Skolnick, “TM-align: a protein structure alignment algorithm based on the TM-score,” *Nucleic Acids Research*, vol. 33, no. 7, pp. 2302–2309, 2005. TM-align.
- [9] D. Bajusz, A. Rácz, and K. Héberger, “Why is tanimoto index an appropriate choice for fingerprint-based similarity calculations?,” *Journal of Cheminformatics*, vol. 7, no. 1, p. 20, 2015. Tanimoto.
- [10] T. Zeevi, R. Shwartz-Ziv, Y. LeCun, L. H. Staib, and J. A. Onofrey, “Rate-in: Information-driven adaptive dropout rates for improved inference-time uncertainty estimation,” in *Proceedings of the Computer Vision and Pattern Recognition Conference*, pp. 20757–20766, 2025.
- [11] A. Schneuing, C. Harris, Y. Du, K. Didi, A. Jamasb, I. Igashov, W. Du, C. Gomes, T. L. Blundell, P. Lio, M. Welling, M. Bronstein, and B. Correia, “Structure-based drug design with equivariant diffusion models,” *Nature Computational Science*, pp. 1–11, 2024. DiffSBDD.
- [12] J. Guan, W. W. Qian, X. Peng, Y. Su, J. Peng, and J. Ma, “3d equivariant diffusion for target-aware molecule generation and affinity prediction,” *arXiv*, 2023. TargetDiff.
- [13] P. G. Francoeur, T. Masuda, J. Sunseri, A. Jia, R. B. Iovanisci, I. Snyder, and D. R. Koes, “Three-dimensional convolutional neural networks and a cross-docked data set for structure-based drug design,” *Journal of Chemical Information and Modeling*, vol. 60, no. 9, pp. 4200–4215, 2020. CrossDocked.
- [14] J. Durairaj, Y. Adeshina, Z. Cao, X. Zhang, V. Oleinikovas, T. Duignan, Z. McClure, X. Robin, G. Studer, D. Kovtun, E. Rossi, G. Zhou, S. Veccham, C. Isert, Y. Peng, P. Sundareson, M. Akdel, G. Corso, H. Stärk, G. Tauriello, Z. Carpenter, M. Bronstein, E. Kucukbenli, T. Schwede, and L. Naef, “PLINDER: The protein-ligand interactions dataset and evaluation resource,” *bioRxiv*, p. 2024.07.17.603955, 2024.
- [15] T. Karras, M. Aittala, T. Aila, and S. Laine, “Elucidating the design space of diffusion-based generative models,” *arXiv*, 2022. EDM.

- [16] S. Dieleman, L. Sartran, A. Roshannai, N. Savinov, Y. Ganin, P. H. Richemond, A. Doucet, R. Strudel, C. Dyer, C. Durkan, C. Hawthorne, R. Leblond, W. Grathwohl, and J. Adler, “Continuous diffusion for categorical data,” *arXiv*, 2022. CDCD Loss.
- [17] Z. Lin, H. Akin, R. Rao, B. Hie, Z. Zhu, W. Lu, N. Smetanin, R. Verkuil, O. Kabeli, Y. Shmueli, A. D. S. Costa, M. Fazel-Zarandi, T. Sercu, S. Candido, and A. Rives, “Evolutionary-scale prediction of atomic level protein structure with a language model,” 2022.
- [18] A. Elnaggar, H. Essam, W. Salah-Eldin, W. Moustafa, M. Elkerdawy, C. Rochereau, and B. Rost, “Ankh: Optimized protein language model unlocks general-purpose modelling,” *arXiv*, 2023.
- [19] W. Ahmad, E. Simon, S. Chithrananda, G. Grand, and B. Ramsundar, “ChemBERTa-2: Towards chemical foundation models,” *arXiv*, 2022.
- [20] Y. Gal and Z. Ghahramani, “Dropout as a bayesian approximation: Representing model uncertainty in deep learning,” in *international conference on machine learning*, pp. 1050–1059, PMLR, 2016.